Cobalt Nanocrystals as Starting Materials for Shape Modification and Assembly Formation

by

Can Kerem Erdonmez

A.B. (Cornell University) 1997
M.S. (University of California, Berkeley) 2001

A dissertation submitted in partial satisfaction of the
requirements for the degree of
Doctor of Philosophy

in

Engineering - Materials Science and Engineering

in the

GRADUATE DIVISION
of the
UNIVERSITY OF CALIFORNIA, BERKELEY

Committee in charge:
Professor Paul A. Alivisatos, Chair
Professor Fiona Doyle
Professor Peidong Yang

Fall 2005

The dissertation of Can Kerem Erdonmez is approved:

Chair Date

Date

Date

University of California, Berkeley

Fall 2005

Cobalt Nanocrystals as Starting Materials
for Shape Modification and Assembly Formation

Can Kerem Erdonmez

Abstract

Cobalt Nanocrystals as Starting Materials
for Shape Modification and Assembly Formation

by

Can Kerem Erdonmez
Doctor of Philosophy in Engineering - Materials Science and Engineering
University of California, Berkeley
Professor Paul A. Alivisatos, Chair

Surfactant-coated cobalt nanocrystals can be prepared with a reasonable degree of control over particle size and shape using a thermolytic route. The small crystallite size, enhanced reactivity and tunable interparticle interactions enable use of this material as a starting material for demonstration of achievement of novel structures using extremely simple solution-based approaches. In particular, formation of hollow cobalt sulfide nanocrystals upon chemical modification and emergence of long-range orientational order upon drying-mediated assembly of cobalt nanocrystals is reported here.

Colloidal preparation of Co nanocrystals has been well-studied. Here, we emphasize general principles and crystallographic/morphological characterization of disk-shaped hcp−Co nanocrystals. Use of surfactant molecules enables achievement of multiple morphologies in one synthetic system.

Formation of hollow structures upon in-solution sulfidation of Co nanocrystals is presented and discussed. A Kirkendall-type effect, involving dominant outward mass transport during formation of the ionic shell material explains the results naturally. It is expected that this phenomenon will generalize extensively to formation of hollow structures

of an enormous variety of compositions. Detailed study of particle morphology as a function of reaction conditions suggest phenomena likely to be generally relevant to use of this approach.

A short report of crystallographic co-alignment into vortex-like structures is also provided. Our current best picture of this process involves an interplay of packing and magnetic interactions between faceted particles.

Professor Paul A. Alivisatos
Dissertation Committee Chair

Dedicated with respect to my colleagues Ben, Giulia and Jason

Contents

List of Figures

Acknowledgments

First, I'd like to thank my adviser, Prof. Alivisatos, who manages, with a light, magic touch, to maintain a civilized yet highly motivated atmosphere in his research group. His creative ideas during group meetings, his frank evaluations of the limits of knowledge in our field and ability to make connections to established work in diverse areas of chemistry and physics have been invaluable for me and my colleagues in our research group. I am grateful to him for giving me a chance to participate in a very exciting field.

I had the good fortune to work with many skilled scientists in Prof. Alivisatos' research group and Lawrence Berkeley National Laboratory. I'd like to thank (chronologically) some mentors and collaborators: Victor Puntes, Daniela Zanchet, Stephen Prilliman, Simon Clark, Tamarack Radetic and Stephen Hughes. Work undertaken in collaboration with several of these people has made its way into this dissertation. Victor discovered the methods for synthesis of cobalt nanocrystals presented here. Daniela and Tamarack are skillful microscopists whose grasp of instrumental issues allowed progress, respectively in characterizing Co nanodisks and in studying assemblies of magnetic nanocrystals. Stephen Hughes has done crucial high-resolution TEM work on hollow nanoparticles.

I worked particularly closely with and owe much to Yadong Yin and Deborah Aruguete. Deborah has been a powerful driving and organizing force in the work on assemblies of magnetic nanocrystals. I believe that her thesis (due in 6 months) will contain improved results and interpretation of our joint, ongoing work. Yadong has not only laid the groundwork for a new method of synthesizing of hollow nanocrystals, but also participated in collection of the data presented here. I also would like to mention that the Alivisatos group seems to have gone through a statistical anomaly; I found most every one of the 40+ people that have come and gone during the time I was a member of the group to be considerate, clear-headed and humorous – I must acknowledge, in particular, Liang-shi Li and Benjamin Boussert as well as (again) Yadong, Deborah and Victor.

Professors Fiona Doyle and Peidong Yang were very accommodating in terms of

setting aside time to revise this dissertation *somewhat* close to the submission deadline. I thank them for their thoughtful corrections.

Last, but not the least, my friends and family have been role models as well as irreplaceable sources of support and advice: Piraye Cönerdem imparted me a small measure of her idealism and stubbornness early in my life; the four other Erdönmez's and Selime have continually kept life interesting; Hui-Ju Wu has been a great source of happiness and wisdom to me during the last 6 years. Elif Pehlivanoğlu, Eren Mantaş, Çağan Şekercioğlu, Katerina Kechris, David Mays, Suzan Yılmaz, Ufuk Kayserilioğlu, Emine Chamberlain and Serin: thank you for your friendship through the years. My last year in Berkeley was improved immensely by various housemates: Esther Budiningrum, Michael Rosenblum, Çağla Meral, Oleksiy Shvets, Shobi Lawalata – I am sorry that I did not get to meet you earlier in my life.

Chapter 1

Introduction

Many phenomena observed in bulk inorganic materials ultimately derive from structures or processes that emerge on length scales spanning several atoms to hundreds of atoms. Accordingly, the last couple of decades have seen a flood of studies on synthesis and characterization of properties for structures with dimensions of 10-500 Å. The basic physical principles motivating study of nanostructures are indifferent to specific synthetic methodology; in practice, however, the mode of production tends to have noticeable consequences in terms of the uniformity, chemical properties and crystalline quality. Thus, choice of preparation method can be a pivotal parameter in studies of material properties.

Colloidal nanocrystals are one important class of nanostructured materials. They are nanometer size crystals, prepared in solution through chemical means, typically with their surfaces functionalized by organic ligand molecules.[3] An ideal sample consists of a population of crystals that is homogenous in size, shape, surface chemistry and crystallographic order. Binding of organic molecules to crystal surfaces during or following synthesis not only prevents aggregation of nanocrystals, but can also inhibit ripening and passivate surface electronic states. An optimized solution-based method for producing ligand-coated colloidal nanoparticles provides a good balance of advantages including sufficient throughput for use of standard characterization tools, some degree of control over size with minor

variations in synthetic procedure and the lack of epitaxial stresses in the free-standing particles produced. The feature that truly sets these particles apart from their gas-phase derived cousins, however, is that a uniform population of as-synthesized, ligand-stabilized nanocrystals approximates a soluble macromolecular species that may immediately be processed in solution or modified chemically.

Nanocrystals of II-VI semiconductors were the first class of colloidal nanostructures where impressive control over size and surface properties were demonstrated.[4] To this day, this system continues to yield impressive refinements in control of nanocrystal shape and properties.[5–9] Progress in this system may be partially attributed to a fortuitous balance between ionicity and covalency as well as presence of two synthetically accessible, epitaxially related polymorphs. In semiconductor nanostructures, quantum confinement effects are noticeable at room temperature in the form of a size-dependent bandgap. Thus, colloidal semiconductor nanocrystals have long recognized as 'artificial atoms' with tunable energy levels, as epitaxially grown quantum dots have been for an even longer time. This analogy motivated early manipulations of the electronic structure of colloidal nanocrystals through surface modification and material choice. Yet, these post-synthesis procedures* themselves were noted by some researchers to underline another analogy: in general, an inorganic nanocrystal is not only a static 'cut-out' of bulk materials, but also a potentially dynamic chemical reagent, like most other known macromolecules.[10]

In contrast to the semiconductor nanocrystals mentioned above, preparation of metallic nanoparticles has had a long but fitful history. While Faraday's preparation and identification of colloidal gold occurred as early as 1858, the next important breakthrough in controlled synthesis, citrate reduction of noble metal salts, occurred around the middle of the 20th century.[11] The size/shape distributions obtained from these methods were not ideal and could not always be improved by size-selective methods due to a tendency

*Including steps such as replacement or removal of ligand molecules, passivation of dangling bond states by surface modification, fabrication of electronic devices by blending nanocrystals with polymers and deposition of nanocrystals from solution onto a substrate.

to irreversibly flocculate. For the several following decades, many recipes were developed; however, each recipe tended to be applicable only to a narrow size range and a specific noble metal.[12] A standard method for preparing stable, monodisperse metal colloids was first realized for synthesis of gold colloids,[13] and was later generalized to synthesis of noble metals. Preparation of colloids of other elemental metals is still a work in progress, with instances of recipes providing good shape/size control being based sometimes on reduction of metal salts and sometimes on thermolysis of organometallic precursors in hot organic solutions.[14] As the Fermi wavelength in metals is usually a few Å, quantum confinement effects are not observable for metallic nanocrystals.[15] Interest in these particles derives from other surface, volume or shape-dependent properties. Magnetic and plasmonic properties of nanocrystals, emerging from collective electronic interactions or excitations and displaying strong sensitivity to surface properties have been two very active areas.[14,16] Size and shape dependence of catalytic efficacy of metallic nanoparticles has also been observed.[17]

As the field of nanocrystal synthesis has progressed, some emphasis has begun to shift from production of simple shapes with theoretically tractable individual properties to the creation and study of more complex geometries and composites of multiple particles.[18] This line of research bears interesting parallels to rational synthesis of organic compounds:[19] thus, creation of branched nanocrystals may be compared with synthesis of dendrimers, attachment of two particles through a linker molecule may be compared with crosslinking or dimerization, aggregation of nanocrystals into ordered arrays is a crystallization process with rather large 'molecules' and so on. Achievement of complex particle geometry or organization of multiple particles into pre-defined structures occurs only rarely[20] as a one-step process; rather, nanocrystals are synthesized in forms constrained by established recipes and then enter a sequence of chemical modification steps as raw materials.

Results detailed in this work fit neatly into this broad picture. Cobalt nanocrystals are synthesized and utilized as suitable starting materials in chemical modification and preparation of highly ordered nanocrystal aggregates. The main body of results concerns

simultaneous compositional/morphological modification of metal nanoparticles.[21] The process presented produces *hollow* nanocrystals of a binary compound with the original metal as one of the components. The shape of the final hollow particle follows closely the shape of the starting *solid* particle. Thus, this process, when generalized, may become one of several 'basic moves' that combine into sequences to achieve complex nanostructures. Observations of hollow particle formation are detailed in Chapter 3. A possible mechanism for the process, based on solid state solution, is provided and related to the Kirkendall Effect[22] whose consequences on length scales ≥ 1 μm are well-known in materials science.[23] Links with previous work in micro- and nanoscale systems are also explored. Finally, a highly simplified model of this process provides some minimal conditions, based on dimensionless parameters, for successful synthesis of hollow structures based on this method. The proposed mechanism yields new questions as to the details of the hollowing process; Chapter 4 contains experimental characterization of nanoparticle morphology and crystallography at different stages of growth. By varying synthesis conditions, clues are obtained concerning processes that, at least in the specific synthetic system studied, add complications to a simple diffusion-based picture.

Work of more speculative nature is presented in Ch. 5 concerning observation of crystallographic co-alignment of nanoparticles upon aggregation into ordered arrays. The results imply an intriguing twist on earlier studies by various groups on producing ordered arrays of nanocrystals. Unfortunately, the most interesting results turn out to be very difficult to reproduce, and a brief discussion of the sensitivity of the structure of aggregates to experimental conditions is included. Possible involvement of packing and magnetic forces among nanocrystals during precipitation is considered employing order of magnitude estimates.

The two separate threads of research covered here, controlled modification of the shape of individual particles and emergence of different degrees of order in particle aggregates, are related by use of a common starting material, cobalt nanocrystals. Therefore,

the next chapter will cover synthesis and characterization of colloidal Co nanocrystals. A brief review of relevant synthetic concepts is covered first. Experimental details, both of the preparation and of the characterization of these particles follow.

Chapter 2

Starting Materials: Synthesis & Characterization

Procedures for preparation of monodisperse metal colloids may be classified on the basis of either the chemical process yielding elemental metals in solution or the mechanism enabling size control. As mentioned in the Introduction, reduction of dissolved metal salts is the most well-established methodology, allowing nanostructures of noble metals (as well as the chemically similar Rh, Pt, Pd, Ir) to be produced with some degree of control over product shape and size. Extension of this approach to more reactive members of the transition series, however, has not always proven simple. During the last decade, thermolysis of organometallic compounds at elevated temperatures has emerged as an alternative, and sometimes superior route for preparing colloids of several important elements and alloys (reviews by Hyeon and Green list many notable recent examples).[24,25] The two approaches are not incompatible: nanocrystals of a binary alloy may be synthesized at elevated temperatures in a one-pot scheme by parallel generation of two metallic species, one from thermolysis, one from reduction.[26] Recently, a promising three-phase (solid-aqueous-organic) procedure capable of producing many elemental, binary and ternary substances was demonstrated.[27] This approach relies mainly on reduction of metal cations, combin-

ing it with ion-exchange between the solid and aqueous phase in a one-pot scheme. This technique has not yet been demonstrated for making colloids of the more reactive metals, such as Fe and Co, that may be required for studies of chemical modification and magnetic properties, such as those presented in the following chapters.

Achievement of size control requires a more detailed discussion. Narrowing of size distributions during growth of colloidal particles has been long known to occur in syntheses of colloidal microparticles. This phenomenon is theoretically possible when sufficient supersaturation of monomeric species* is maintained during growth of particles in solution.[28,29] An additional requirement for achievement of monodisperse samples is that nucleation of particles be confined within an interval at the beginning of synthesis and not overlap significantly with particle growth (see Fig. 2.1). Seeding of the synthetic solution with small particles and subsequent growth under monomer supersaturation allows for reconciliation of these requirements by separating nucleation and growth processes. A one-step scheme, elucidated by La Mer and Dinegar,[1] provides a conceptually more complicated, but experimentally simpler solution to the same problem: a very high supersaturation is realized at the beginning of synthesis and yields an initial burst of nucleation. Subsequently, monomer concentration falls sharply to a value that is too low for further nucleation of particles, but large enough for narrowing of the particle size distribution. Many recipes for synthesis of monodisperse nanocrystals employ conditions where this mechanism may be expected to operate. Size distributions have indeed been shown to sharpen upon injection of small amounts of dissolved precursor into a hot colloidal solution of II-VI or III-V nanocrystals, providing convincing support for 'focusing' of particle sizes during growth.[30] Continuing to hold a solution of these nanocrystals at the elevated synthesis temperature after monomeric species have been consumed was seen to lead to degradation of the size distribution by

*Some terminology: the reagent introduced into the synthetic system by the experimentalist that acts as the source of metallic species is referred to as the *precursor*. The species which ultimately condenses to nucleate/grow colloidal particles is referred to as the *monomer* or the *monomeric species* . The monomeric species could be the precursor, but in general will not be.

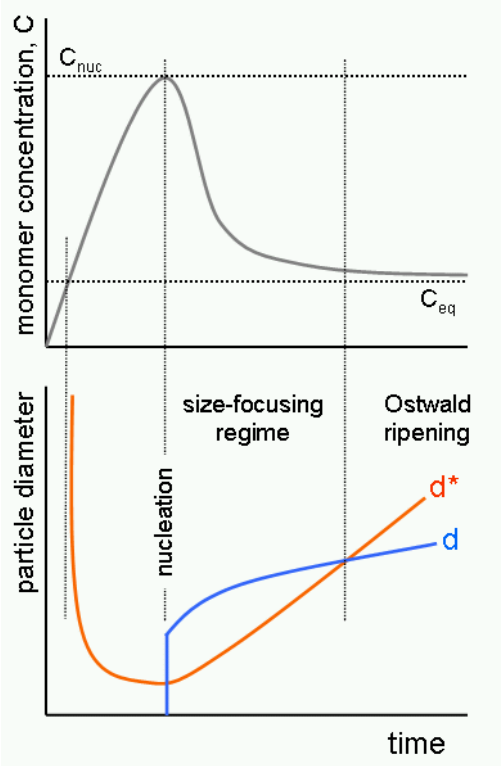

Figure 2.1: Schematic mechanism for size-focusing in one-pot syntheses, adapted from LaMer.[1] (Top) Initially, monomer concentration, C, increases through addition or decomposition of precursor. When C reaches C_{nuc}, a burst of nucleation occurs. Subsequently, C falls sharply towards the monomer solubility at equilibrium, C_{eq}. (Bottom) Minimum size of nuclei, $d^{\star}$, allowed to form at a given time is inversely proportional to $(C - C_{eq})$. In an idealized picture, nucleation is accomplished within a very brief time. Afterwards, particles grow by consuming monomer, slowly reducing C towards C_{eq} and increasing $d^{\star}$. 'Size-focusing' may occur over the interval for which $d > d^{\star}$.

Ostwald ripening.

The much higher surface-to-volume ratio of nanocrystals (in comparison to μm-size particles) tends to require a larger input of free energy into the synthetic system, in the form of highly reactive precursors and/or elevated temperatures. Compressed timescales for size-focusing, Ostwald ripening and particle coalescence often result, making manual, reproducible control of nanocrystal size challenging. Addition of organic molecules that bind to nanocrystal surfaces during growth lowers excess surface energy and can have a tremendously beneficial effect on the facile achievement of size control. Surface passivation of particles not only inhibits unintended aggregation or coalescence of particles during growth, but also dictates final particle size through a strong influence on the energetics of the nucleation process and kinetics of growth.[3,26]

When size control cannot be achieved in a simple manner by a combination of size-focusing and surfactant regulation of nucleation and growth, more complicated experimental approaches may be considered. A notable route is preparation of water-in-oil droplets stabilized by surfactants and use of these droplets as nanoscale reactors and/or synthetic templates. Several drawbacks of this technique have been discussed, most notably the possibility of surface contamination by organics or oxides, generally poor size distributions of particles produced and possible destabilization of micelles by reactive/concentrated reagents.[3,31,32] In some exceptional cases, use of procedures that statistically separate nanocrystals on the basis of size have been employed to obtain high-quality, monodisperse fractions from as-synthesized samples.[33,34] Use of post-synthesis size-selective methods is not limited to micellar preparations; these methods have also been applied to narrow size distributions for samples prepared by thermolytic or reductive routes in organic solvents.[3,14] While size-selection may be a powerful tool, the broader the size distribution for as-synthesized samples, the greater the extent of fractioning required to obtain monodisperse samples. Thus, a narrow size distribution of as-synthesized nanocrystals still remains highly desirable for achieving a good yield of nanocrystals of the desired size.

2.1 Overview: Cobalt Nanocrystal Synthesis

Interest in elemental and alloyed nanocrystals of transition metals such as Ni, Fe, Co has been driven by their magnetic properties as well as potential catalytic uses. For applications of nanocrystals in data storage or magnetic functionalization of biomolecules, elemental cobalt is not an optimal material due to its relatively low coercivity and tendency to oxidize. Still, recipes for making colloidal cobalt have turned out to be excellent first steps towards production of alloyed/intermetallic cobalt compounds that are oxidation-resistant and have high coercivities.[26] More importantly from a fundamental point of view, colloidal cobalt has turned out to be an extremely rich synthetic system. Relatively uniform samples of different morphologies and phases have been realized in the literature, novel results sometimes deriving from a small changes to an existing recipe.[35,36]

Table 2.1 lists some syntheses of Co nanoparticles found in the literature. Thermolytic routes for production of colloidal cobalt are among the oldest for preparation of ferrofluids, but achievement of narrow particle size distributions at the nanometer scale was achieved only recently. The diversity of the phases and shapes of colloidal cobalt particles that can be achieved is striking considering the elemental composition of the product. Both reductive and thermolytic routes have been employed. The shapes achieved are a strong function of the composition of the solvent/surfactant mixture. Most interestingly, at least three crystallographic phases are accessible by one-pot methods. One common thread is that temperatures higher than room temperature are needed to produce single-crystalline nanoparticles. This has been noted to be quite a general phenomenon for crystallization of (non-noble) transition metals in solution.[3] Another common finding is that size distributions for as-synthesized nanocrystals tend to be too broad for study of highly volume-dependent properties. This is commonly remedied by size-selective methods based e.g. on preferential precipitation of larger particles or magnetophoresis of nanocrystals. A small number of methods are capable of producing essentially monodisperse ($\leq$10%) products without

recourse to size-selection. In these cases, the exact choice of the surfactant mixture seems to play a critical role.

The recently identified crystallographic phase of $\epsilon-$Co merits special mention, as most of the results presented in the following chapters make use of nanocrystals of this material. Dinega and Bawendi were able to synthesize this phase in colloidal form in 1999 by decomposing $Co_2(CO)_8$ in toluene slowly heated to its boiling point in the presence of trioctylphosphine oxide (TOPO).[45] The colloidal particles produced were quite polydisperse and 20 nm in diameter on average. Analysis of X-ray diffraction patterns demonstrated the nanocrystals to adopt a complex cubic structure previously known to be adopted by a high temperature phase of manganese ($\beta-$Mn), but not by cobalt. Interestingly, the same preparation without TOPO yielded fcc$-$Co. Later synthetic variations by Sun and Murray,[44] as well as Puntes et al.[47] showed that use of neither $Co_2(CO)_8$ nor TOPO are essential for formation of $\epsilon-$Co. In fact, Puntes' results suggest that hcp$-$Co nanocrystals will transform into $\epsilon-$Co in an organic solvent at elevated temperature (T$\sim$180°C) within minutes.

Despite a distinct, complex crystal structure (Fig 2.2), $\epsilon-$Co is similar to other forms of cobalt in terms of the few properties measured. Its density (8.64 g/cm^3) is only 2.5% smaller than that of close-packed forms. The magnetic moment of 1.7 μ_B per atom is similar, within error, to values known for hcp$-$Co (1.72 μ_B) and fcc$-$Co (1.75 μ_B). Diluted suspensions of $\epsilon-$Co nanocrystals of diameter $\sim$10 nm reveal them to be superparamagnetic at room temperature and the magnetic behavior of dilute colloids are consistent with a magnetocrystalline anistropy about 60% of that observed for close-packed forms. This is in contrast to $\beta-$Mn where an identical crystal structure (except for a slightly larger lattice parameter) is argued to suppress magnetic ordering due to geometrical frustration despite antiferromagnetic interactions between magnetically active atoms.[2,49,50]

Ref.	Reagents	Solvent	Surfactant	T(°C)	Shape	Size(nm)	Phase	σ(%)
[37]	$Co_2(CO)_8$	toluene	copolymer	110	sph./cube	2–30	fcc	>15
[38]	$Co_2(CO)_8$	toluene	various	110	sph./cube	5-100	mt-fcc	>20
[39]	$Co_2(CO)_8$	toluene	AOT	110-140	?	6-11	?	>10
[40]	$CoCl_2$+$NaBH_4$	H_2O/isooctane	AOT	?	?	1.5-4.5	amr.	?
”	”	toluene	DDAB	?	?	7-13	?	?
[41]	Co^{2+}+N_2H_4	H_2O (pH>7)	none	?	disk	15x100	hcp	>20
[42]	$Co(CO)_3(NO)$	decane	OA	0	sph.	5-10	amr.	>25
[43]	$Co_2(CO)_8$	p-xylene	PAS/NaAOT	125-170	sph.	7-17	?	>20
[44]	$CoCl_2$+$LiBEt_3H$	dioctylether	OA+TAP	200	sph.	2-11	$\epsilon-$Co	$7^{\dagger}$
[45]	$Co_2(CO)_8$	toluene	TOPO	110	sph.	20	$\epsilon-$Co	15
”	”	”	none	110	?	?	fcc−Co	?
[46]	$Co(AOT)_2$+$NaBH_4$	H_2O	NaAOT	none	sph.	7	amr.	10
[47]	$Co_2(CO)_8$	dichlorobenzene	OA+TOPO	180	sph.	3-16	$\epsilon-$Co	<10
[48]	$Co(CH_3COO)_2$+1,2-dodecanediol	phenylether	OA/TAP	240	sph.	2-12	hcp	10
”	$Co_2(CO)_8$	phenylether	OA/TBP	200	sph.	7-10	mt-fcc	?
[35]	$Co_2(CO)_8$	dichlorobenzene	OA+AA	180	disk	2x4 - 4x90	hcp	> 25
[36]	$[Co(\eta^3\text{-}C_8H_{13})(\eta^4\text{-}C_8H_{12})]$+$H_2$	anisole	OA+AA	150	sph→rod*	3→6x120	hcp*	?

Table 2.1: Some syntheses of colloidal Co found in literature. The size distribution, when not reported and when possible, was estimated casually from published TEM images. σ: fractional standard deviation of the nanocrystal size distribution, referring in the case of disk-shaped particles, to diameter, not thickness, AOT: bis-(2-ethylhexyl)sulfosuccinate, PAS: poly(acrylo-nitrile) copolymer, TAP: various trialkylphosphines, TBP: tributylphosphine, OA: oleic acid, TOPO: trioctylphosphine oxide, sph.: spherical, amr.: amorphous, mt-fcc: fcc crystal structure with multiple twinned crystal domains present in an average particle.

(*): transformation of small spheres to rods and wires took place over 48 hours

(†): size-selective precipitation was employed to achieve this distribution.

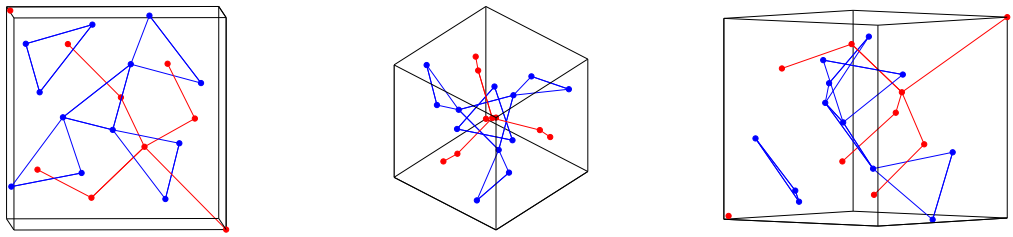

Figure 2.2: Different views of the crystal structure of $\epsilon-$Co. Viewing down a direction near (left) (0 0 1), (middle) (1 $\bar{1}$ 0), (right) (1 1 1). The three views are roughly orthogonal to each other. The two different colors correspond to the two different types of Co atoms located in distinct bonding environments. Each atom is shown with a line connecting it to its nearest neighbors of the same type. Note the 'windmill' arrangement adopted by nearest-neighbor triangles of the blue atoms.[2]

2.2 Basic Synthetic Procedure

Cobalt nanocrystals used in the studies described in the following chapters are synthesized according to a published procedure based on thermolysis of an organometallic precursor.[47] A weakly polar substance, o-dichlorobenzene (DCB hereafter) is chosen to be the solvent. The organic ligands utilized vary from synthesis to synthesis. A mixture of oleic acid and trioctylphosphine oxide (TOPO) is the most common combination of ligand molecules; long chain primary or tertiary amines may be used in addition to or as a substitute for these ligands. In a typical synthesis, 0.25 mmols of TOPO are degassed in a large round bottom flask under stirring, by heating to 50°C under flowing Ar for 20 minutes. Argon flow and stirring are maintained through the rest of the synthesis. A similar amount (0.3 mmol) of oleic acid stored in air-free conditions is dissolved in 15 ml of DCB in an Ar-filled glovebox. The solution is added, using air-free techniques, into the flask and heated to its boiling point (182-185°C). In the meantime, 3.15 mmols of the cobalt precursor, $Co_2(CO)_8$ is dissolved in 3 ml of DCB in the glovebox and sealed in a vial. When the DCB/surfactant mixture reaches refluxing conditions, the precursor solution is withdrawn into a syringe and rapidly injected into the flask.

Thermal decomposition of $Co_2(CO)_8$ into Co and carbon monoxide is extremely rapid at this temperature, evidenced by a short burst of CO evolution from the solution. The temperature of the solution drops to 160-170°C following injection, due to the endothermic nature of the decomposition reaction and/or the addition of a small amount of cold solvent. Heating is maintained following injection and the temperature climbs back to the injection temperature within 1 min. Aliquots may be withdrawn from solution at different times following injection and allowed to cool to room temperature in a sealed vial. The solution thus collected is invariably ferrofluidic, moving even against the force of gravity, towards a magnet brought into its proximity.

Characterization of the product may be performed employing a combination of transmission electron microscopy (TEM) and X-ray diffraction (XRD). Sample preparation for microscopy is very simple: a drop of the solution is placed onto a TEM grid and covered with a Petri dish. The solvent evaporates slowly (>30 minutes for complete drying), allowing nanocrystals to aggregate into ordered structures. Preparation of powder samples for XRD analysis requires precipitation of particles from solution. Methanol dissolves readily in DCB, increasing the polarity of the solution. There is a resulting decrease in the solubility of nanocrystals coated with ligand molecules with hydrophobic tails; turbidity and precipitation on vial walls may be noticed immediately upon addition of methanol. Adding an equal volume of methanol to an as-synthesized sample and centrifuging for 5-15 min at 4000 rpm precipitates most nanocrystals. The supernatant is discarded and the precipitate is dried by flowing dry nitrogen over it for 1 hr or longer. The supernatant is usually clear and colorless, indicating complete reaction and complete precipitation. Rare observations of a clear but colored (blue or pink) supernatant may indicate presence of cobalt complexes, with either organic molecules or water. In other cases (also rare), the supernatant is clear and brown or gray despite repeated centrifugation – the color may be due to unconsumed cobalt carbonyl or nanocrystals solubilized in polar environments by formation of a double surfactant layer around them.

TEM images confirm that nanocrystals are present in aliquots collected 'instantly' from solution (in practice, collection and cooling of an aliquot cannot occur faster than 15-30 secs). The size and shape distribution of particles can be tracked as a function of time elapsed following injection (Fig. 2.3 shows TEM images of particles synthesized at a slightly lower temperature where evolution of particle shape and size can be tracked more easily within a single synthesis). Samples collected 1-5 minutes following injection show spherical nanocrystals with fair (∼15%) to excellent (∼5%) size dispersion (measured from TEM images as the ratio of standard deviation of nanocrystal diameter to average diameter). A narrow size distribution correlates strongly with aggregation of nanocrystals into ordered 2- and 3-dimensional arrays on the TEM grid (Fig. 2.3). As time at reflux temperature before collection increases beyond ∼10 min, the nanocrystal size distribution degrades in a manner consistent with a combination of Ostwald ripening, nanocrystal coalescence and annealing: maximum particle size increases with time and faceted particles appear alongside apparently spherical particles. Typically limited or no Ostwald ripening takes place during thermolytic synthesis of metallic nanoparticles due to the highly irreversible reactions employed and low solubility of metallic species in organic solvents.[26] Observation of Ostwald ripening in this system is best attributed to presence of TOPO, believed to enable atom exchange between particles by complexing Co atoms.[47]

XRD patterns show that particles are crystalline and belong to the recently identified $\epsilon-$Co phase.[45] Usually, no evidence of oxides of Co is seen in the patterns despite exposure of sample to air for 20-120 min during data collection. When an oxide is observed, it is in the form of very broad peaks that correspond in position to major CoO diffraction peaks. Significant broadening of $\epsilon-$Co peaks beyond instrumental broadening is observed in the patterns. The Debye-Scherrer equation may be used to roughly estimate the average size of a crystalline domain based on linewidths. With appropriate parameters for the

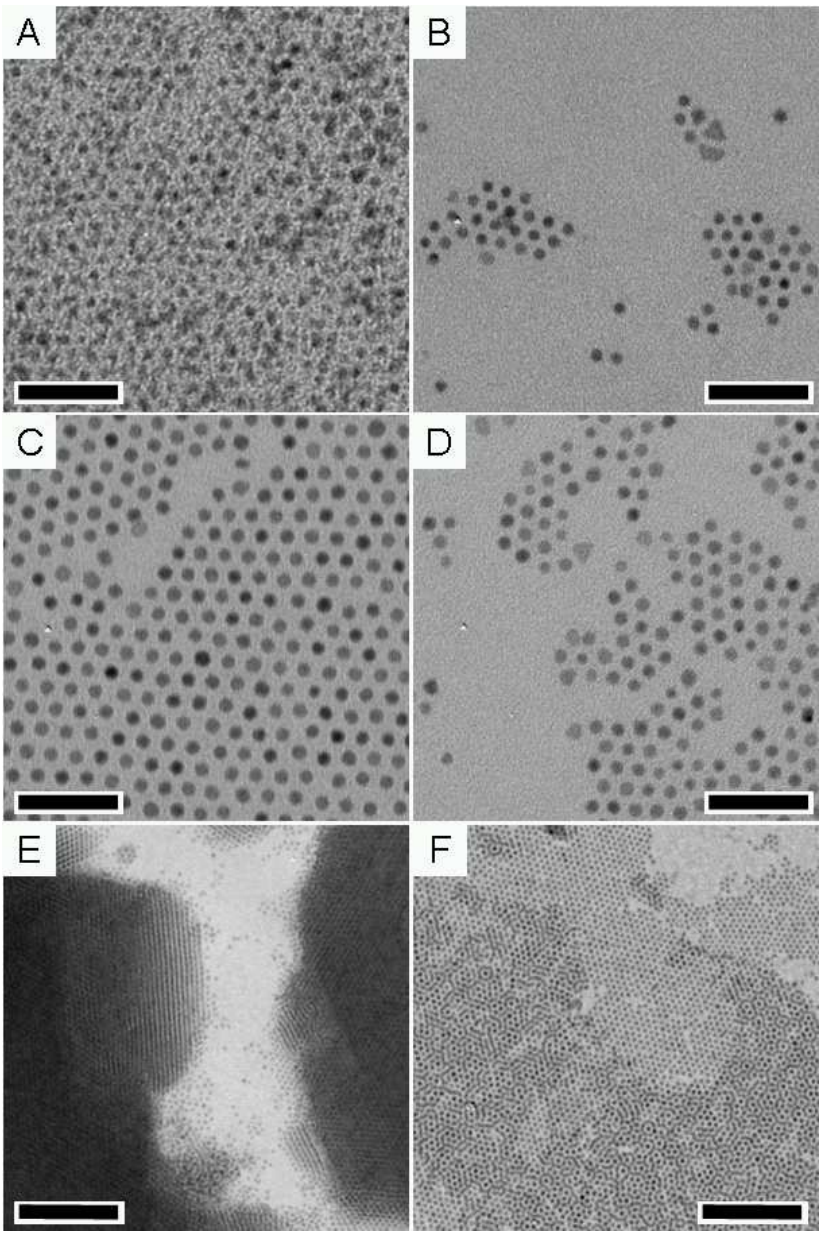

Figure 2.3: (A-D) TEM of $\epsilon-$Co spheres held in DCB at 160°C respectively for 2, 5, 10 and 15 minutes following injection of $Co_2(CO)_8$ into DCB at 170°C. The lowered temperature allows a demonstration of initial improvement and slow degradation of the uniformity of the nanocrystal population with time. The relatively monodisperse nanocrystals displayed in (C) are seen to assemble upon drying into thick three-dimensional ordered lattices in (E) and mono- and bilayers in (F). The scale bars correspond to 40 nm for (A-D) and 200 nm for (E,F).

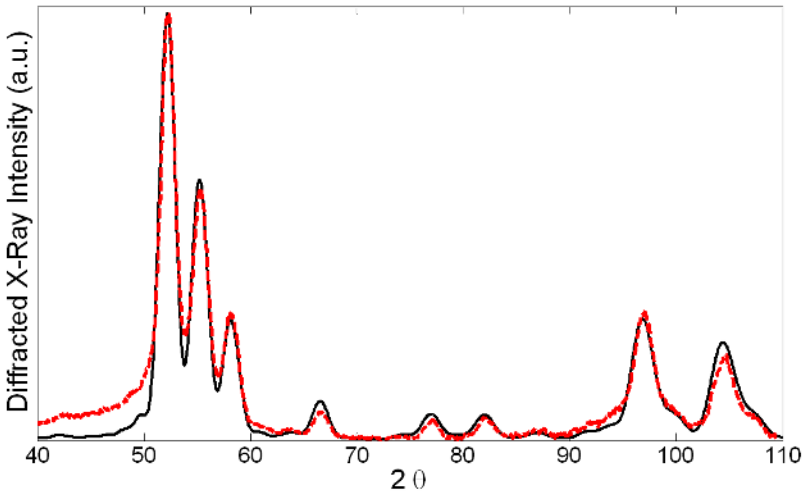

Figure 2.4: Experimental XRD patterns (dashed red curve) of spherical $\epsilon-$Co particles confirm that they are composed of $\epsilon-$Co and are crystalline. Simulated patterns (black curve) must be compared to the experimental curve to establish the single-crystalline nature of the nanocrystals. The simulated curve here is for 7.3 nm spherical $\epsilon-$Co crystals and matches experiment well. TEM shows 8-9 nm nanocrystals, the difference in size being attributable to a thin oxide/amorphous/surfactant shell that is visible in electron imaging, but does not contribute to diffraction patterns.

diffractometer used, crystal domain size in nanometers is roughly,

$$D(nm) \sim \frac{10^{\circ}}{FWHM}$$

where FWHM is the full width at half maximum in degrees for a diffraction line on an intensity vs. 2θ plot. The peaks in recorded diffraction patterns have peak widths ($FWHM$) of 1-2°, corresponding to 1-2 crystal domains in an average nanocrystal. A simulation method described in the literature allows for more precise determination of the average size and shape of nanocrystals from XRD data.[51–53] This method was adopted to calculate XRD patterns expected from various assumed nanocrystal shapes and sizes. The simulation methodology is based on kinematical rather than dynamical diffraction theory, neglecting absorption and intensity oscillation effects that must be taken into account for thick samples composed of large crystal domains. Briefly, an expression for the contribution to the

diffraction intensity due to interference between two atoms is summed over every pair of atoms (not necessarily neighbors) in a spherical nanocrystal.[54] Line broadening due to thermal disorder and radial strains is likely to be negligible in comparison to size-broadening; thus all atoms are assumed to be located at ideal positions given by translation of the unit cell contents. Assuming all nanocrystals to have a domain size very similar to the average nanocrystal diameter observed in TEM images provides a decent fit to the peak widths, confirming that most particles are single crystalline (Fig. 2.4).

2.3 Synthesis: Variations and Limitations

Disk-shaped cobalt nanocrystals were prepared using a variation of the above recipe.[35] The surfactant mixture employed was the one described in the previous section except for the addition of a significant amount (2.5 mmol) of hexadecylamine. Nanocrystals thus produced appear in TEM images typically as long linear arrangements of parallel rods. The non-spherical particle shape can be attributed to preferential attachment of amines onto particular crystal facets during growth, leading to anisotropic growth of nanocrystals. TEM imaging of a set of nanocrystals, tilting the specimen holder and re-imaging the same nanocrystals allows one to establish the three-dimensional shape of the nanocrystals. The results shown in Fig. 2.5 establish that the aligned nanocrystals are not rods, as they seem to be in projection, but correspond to stacks of disks lying on the substrate on their sides. The disks have thicknesses in the range 2-4 nm (this number is difficult to estimate, due to a varying degree of tilting and contrast for particles that stand almost, but not quite, on edge on the substrate. The diameter distribution is extremely wide, spanning 5-50 nm and appearing to be multimodal. At first glance, XRD patterns collected for these particles seem to match the $\epsilon-$Co phase observed for the spherical particles obtained in amine-free syntheses. This is unexpected based on the cubic and apparently fault-free nature of the $\epsilon-$Co structure, as growth of uniaxial crystals would seem to require breaking cubic sym-

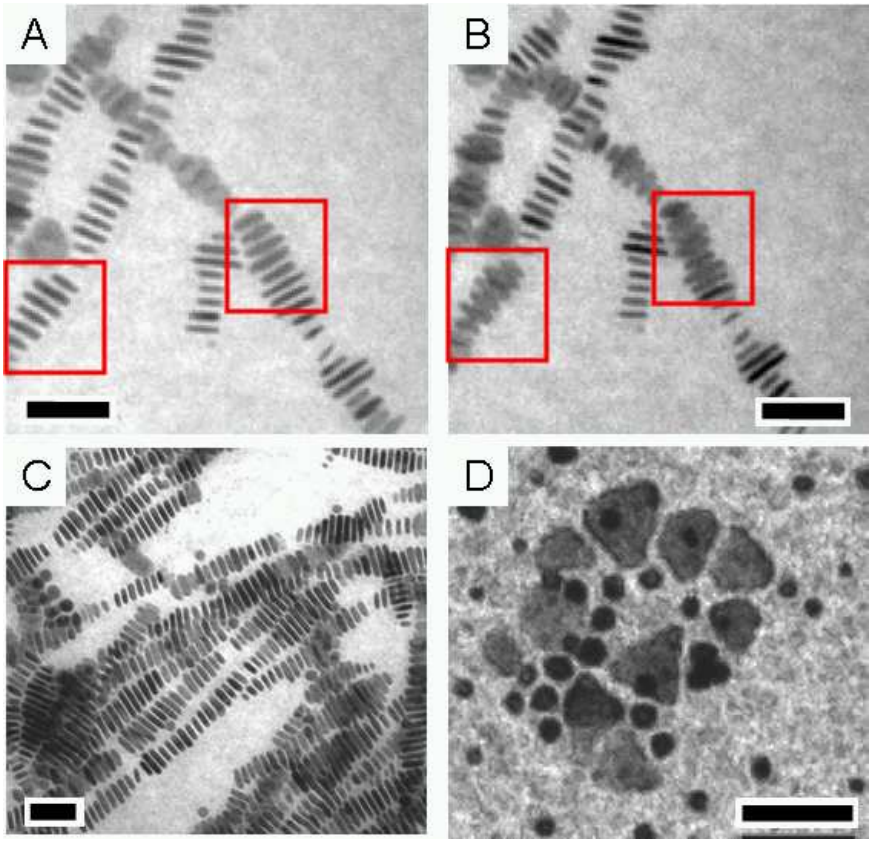

Figure 2.5: (A,B) TEM images of hcp−Co disks before and after tilting (20°). Nanocrystals marked with red boxes are seen to change in appearance upon tilting, implying that the nanocrystal shape is *not* rod-like. (C) Disks stack into long linear structures, maximizing particle-particle contact. (D) Larger particles are usually faceted and more transparent to electrons than smaller round particles, implying a mixture of spheres and disks in the sample. The scale bars correspond to 50 nm. ()

metry. Careful examination of the patterns reveal a couple of weak but sharp peaks at positions associated with fcc or hcp phases of Co. Going back to TEM images, apparently round particles are seen to form two separate populations. One set of particles appears relatively darker, despite being limited to diameters of $\leq$12 nm. The second set of particles is much more transparent to electrons even for diameters >40 nm (see last panel in Fig 2.5). These thin particles also sometimes display triangular faceting. This suggests that apparently round particles are a mixture of spherical $\epsilon-$Co nanocrystals and significantly thinner disks of either hcp$-$Co or fcc$-$Co lying flat on the substrate.

The hypothesized presence of two nanocrystal shapes, each associated with a different crystallographic phase, warrants inspection of the XRD data with an eye towards possible combinations of particle shape and size. Accordingly, simulations of XRD patterns expected from hcp$-$Co, fcc$-$Co and $\epsilon-$Co nanocrystals with disk-like, rod-like or spherical shapes were performed. Qualitatively, experimental patterns best match, among the cases considered, a mixture of a 'minority' of hcp$-$Co disks with a majority of $\epsilon-$Co spheres. When a magnet is brought close to a solution containing Co nanodisks, instead of the whole solution moving towards a magnet, as observed in pure solutions of Co nanospheres, filaments of a shiny black material precipitate out of solution and move towards the magnet. These filaments aggregate and collect on the spot on the inner vial wall closest to the magnet. The tendency of disks to stack into linear arrangements observed in TEM images is presumably amplified in the presence of a magnetic field, resulting in the characteristic formation of the filamentous precipitates. This behavior was used to repeatedly separate the filaments and redissolve them in fresh solvent, yielding a sample where peaks attributed to hcp$-$Co have been enhanced in the XRD pattern (Fig. 2.6). Disk-shaped particles may thus be assigned to the hcp$-$Co phase. HRTEM imaging seems to confirm this assignment.[35] Furthermore, Gibson's synthesis of large Co disks (15x100 nm) of a modified hcp phase using hydrazine as a reducing agent also supports this identification.[41] The undetermined disk thicknesses, the very broad diameter distribution and the presence of multiple

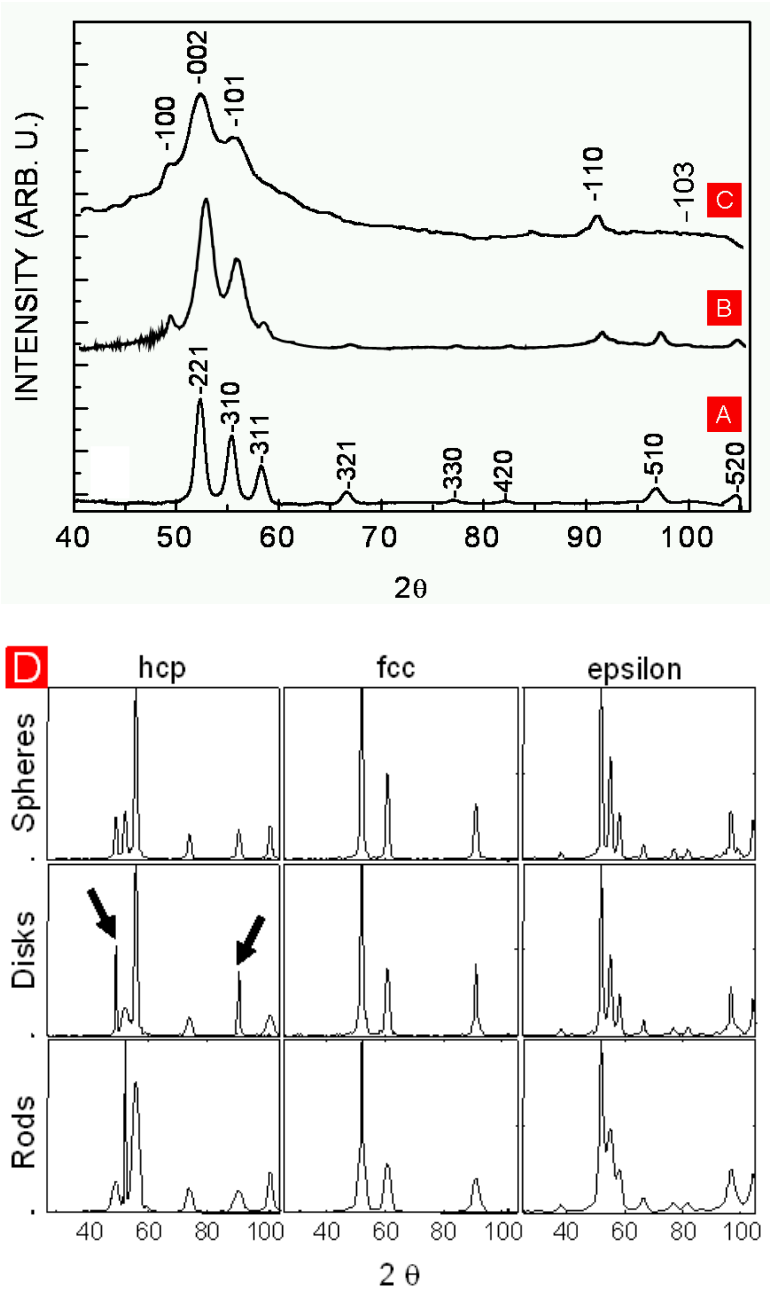

Figure 2.6: Observed and simulated patterns for a disk/sphere mixture synthesized using linear amines as surfactant: (A) experimental pattern for an $\epsilon-$Co sample included for reference, (B) experimental pattern for an as-synthesized sample, (C) pattern of the same sample after being subjected to repeated magnetic separation. Peaks of hcp$-$Co are labeled on this pattern. Evolution from a $\epsilon-$Co-like diffraction pattern to an hcp$-$Co-like pattern is evident, (D) composite plot of simulated XRD intensities for 3 possible phases (hcp, fcc, $\epsilon-$Co) and 3 possible shapes (11 nm spheres, 20x4 nm disks and 4x20 nm rods) that may be expected for Co nanocrystals. Arrows mark hcp$-$Co peaks visible in (B) and (C).(© American Chemical Society)

phases and morphologies makes collection of particle statistics for disk-containing samples very difficult. More importantly, the presence of very different particles in the nanocrystal population may result in further and intractable amplification of sample heterogeneity upon further modification of these particles. This limitation is borne in mind and only qualitative inferences based on morphology of single particles are made when cobalt nanodisks are used as starting materials for chemical modification (see Ch. 4).

Spherical cobalt nanocrystals prepared according to the standard recipe described in the previous section are much easier to characterize. Thus, it is possible to look for relationships between the average properties of a solution of these particles and the properties of structures derived from them. Still, it must be noted that the nanocrystal size distribution varies noticeably from synthesis to synthesis. In practice, the variation that is most difficult to characterize turns out to be the presence of a minority of smaller particles (3-5 nm) alongside larger (7-10 nm) particles of measurably narrow dispersion (Fig. 2.7). The occurence of a bimodal size distribution can be attributed to the initial drop and subsequent rise in solution temperature following injection of carbonyl.

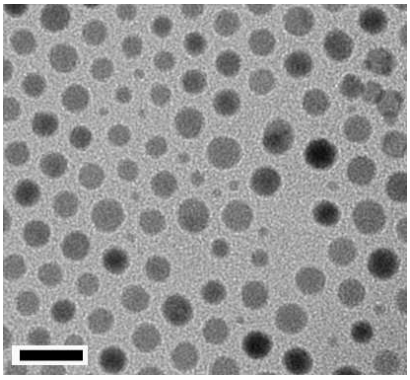

Figure 2.7: A synthesis in which a subpopulation of small (∼1-3 nm nanocrystals) were produced alongside larger $\epsilon-$Co spheres. Scale bar: 20 nm.

These particles present much lower contrast in comparison to larger ones. Thus, their sizes and relative numbers are difficult to estimate. In cases where cooling of the sample before further manipulation is acceptable, particle size distributions can be improved through size selective precipitation. The method is the same one used for precipitating nanocrystals for preparation of XRD samples. In this case, it is desired to precipitate larger particles only, rather than all particles. Therefore, a smaller amount of methanol (e.g. 0.3 ml/ml of DCB) is added to the as-synthesized solution. The supernatant is separated and the

precipitate, containing on average larger particles, is redissolved in pure solvent. Further separation may be performed repeatedly on the fractions obtained, yielding a series of samples separated according to average particle size. For samples with a good size distribution except for the presence of a sub-population of small particles, one or two separation steps suffice to obtain monodisperse samples of the larger particles. This strategy is employed to prepare the highly monodisperse samples required for formation of highly ordered superlattices upon drying of colloidal solutions covered in Ch. 5.

In the next couple of chapters, we will cover results relating mostly to sulfidation of cobalt nanocrystals in an organic solution. In principle, it is best to avoid variations in thermal history or chemical environment between each synthesis of nanocrystals and the following sulfidation step. This minimizes variations in surface chemical properties from synthesis to synthesis, allowing general trends to be established. Furthermore, precipitation/redissolution or cooling/reheating of cobalt nanocrystals were often seen to result in aggregation as well as diminished uniformity for structures obtained by sulfidation of the nanocrystals. Thus, utilization of size selective methods or reheating of a sample confirmed by TEM to be monodisperse were not available options for these studies. Instead, variations in the size distribution of the starting materials from synthesis to synthesis are accepted and characterized by collecting a small aliquot of the hot nanocrystal solution prior to sulfidation. By producing cobalt nanocrystals and sulfidizing them in a one-pot scheme, we can prepare stable solutions of nanoparticles with a well-defined, hollow geometry.

Chapter 3

Synthesis of Hollow Nanoparticles via the Kirkendall Effect

Nanocrystals of a reactive metal might be expected to undergo rapid chemical transformation in presence of an oxidizing species. However, it is known from studies of oxide film formation on metals that several interdependent processes* combine to determine the extent and speed of film growth, as well as the final morphology adopted by the film. Noticeable variation in growth mechanism and kinetics for different choices of reactants may thus be expected also for film growth on nanocrystals. More interestingly, the film (or if reaction proceeds to completion, the particle) morphology may vary accordingly, potentially resulting in varied shapes, porosity, roughness, mechanical or chemical stability as a function of synthesis conditions. Reports of oxidation kinetics for nanocrystalline aggregates of metallic particles exist in the literature,[55] but the state of aggregation is likely to influence the observed results strongly in such studies. A recent study on isolated Si nanocrystals deposited on a graphitic surface showed enhanced short-term and slowed long term oxidation kinetics in comparison to the oxidation behavior of bulk Si, attributing the difference specif-

*e.g. diffusive and charge transport of reactants, defect formation and migration, lattice or thermal mismatch between the substrate.

ically to the spherical oxidation geometry.[56] Important observations of chemical/structural modification of nanocrystals were reported recently, for example, change of crystallographic phase upon change of solvent,[57] diffusion-limited oxidation of maghemite nanocrystals in water[58] and complete, shape-preserving cation exchange on colloidal CdSe nanocrystals to yield Ag_2Se nanocrystals.[59] Despite the gentle chemistries employed, these transformations proceed at dramatically higher rates and lower temperatures than observed or expected in bulk materials. The enhanced kinetics and/or reactivity were attributed to the smaller diffusion lengths, the presence of a disordered 'reaction front' spanning a large fraction of each nanocrystal and sensitivity of internal bonding on surface chemistry. Thus, the size of nanocrystals enables their transformation in relatively mild conditions where solution chemistry may be employed. The mild conditions and solution methods, in turn allow for homogenous modification of each isolated nanocrystal in a colloidal sample, removing complications that arise when aggregates of nanocrystals are used as starting materials. This chapter describes another instance of complete chemical (*and* morphological, in this case) transformation of nanocrystals in solution: colloidal $\epsilon-$Co is reacted with molecular sulfur to obtain hollow sulfide shells. The hollow geometry obtained and the final composition of the product turn out to be simple to describe. Furthermore, formation of the hollow geometry finds a feasible explanation in diffusive processes already known to influence microstructures derived from solid-state reactions or interdiffusion of metals. After presentation of the results, some relevant, prior work from the literature is reviewed. Formation of hollow nanocrystals upon chemical modification is qualitatively explained within a picture of dominant, outward cobalt diffusion during sulfidation. The few quantitative results presented, however, point to some complications to that idealized picture. Experimental support for and in-depth discussion of these additional processes is delayed until the following chapter.

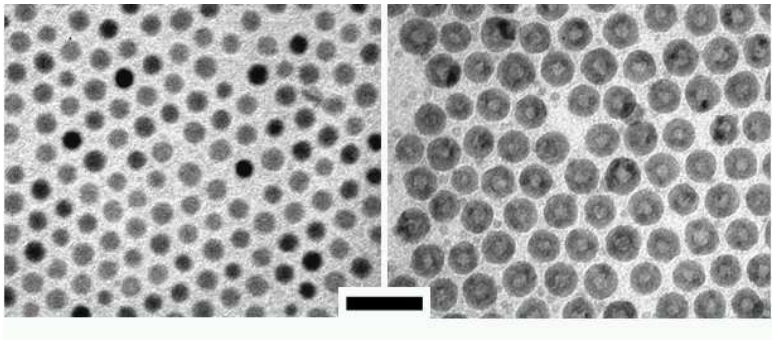

Figure 3.1: (A) $\epsilon-$Co nanocrystals 1 min. after $Co_2(CO)_8$ injection. (B) Same solution, collected 1 min. after injection of sulfur dissolved in DCB. The scale bar is 50 nm. (© American Association for Advancement of Science)

3.1 Sulfidation of Cobalt Nanocrystals

The original preparation of hollow sulfide shells was serendipitous.* However, in retrospect, molecular sulfur is a good choice for an oxidizing species: moderate amounts of it can be dissolved in several organic solvents, in contrast to other electronegative elements which may be gaseous, requiring continual bubbling to achieve at most low concentrations in solution or which may adopt insoluble polymeric forms.

Synthesis of hollow shells proceeds simply. Spherical nanocrystals of $\epsilon-$Co are prepared in refluxing *o*-dichlorobenzene (DCB) as described in the previous chapter. Within a short interval ($\sim$1 min) of injection of $Co_2(CO)_8$ and formation of cobalt nanocrystals, molecular sulfur dissolved in a small amount of dichlorobenzene is injected into the solution. There is no appreciable color change or noticeable reaction upon injection. However, for aliquots collected almost instantly following injection of sulfur, a well-defined hollow morphology is adopted by the vast majority of nanocrystals seen in TEM images (Fig. 3.1).

3.1.1 Crystallography

It is natural to assume that the hollow particles thus produced are composed of cobalt sulfide. However, many different binary compounds of cobalt and sulfur exist.

*The synthesis and observation are due to Yadong Yin, who at the time intended to cross-link the surfactant coating on cobalt nanocrystals to improve their stability.

Furthermore, it is not clear, based only on TEM images, whether nanocrystals collected after a specific time at the reaction temperature correspond to products of a completed reaction. XRD of a dried powder of the hollow particles (prepared in a manner identical to the one described for Co nanocrystals in the previous chapter) confirms that they are composed of nanocrystalline cobalt sulfide. More specifically, when the number of S atoms added equals the total number of Co atoms already in the nanocrystal solution, XRD patterns of hollow nanocrystals collected within $\geq$15 sec. of injection index unambiguously to the mineral cobaltpentlandite, with the composition Co_9S_8. No sign of $\epsilon-$Co is observed in the patterns, suggesting complete (or at least near complete) consumption of metallic cobalt (Fig. 3.2).

Three different phases of cobalt sulfide are known to be stable at room temperature in bulk form. Thus, we attempted to synthesize different phases of cobalt sulfide by varying the S:Co ratio. Increasing this ratio to values over 4:3 resulted in samples consisting purely of linnaeite, Co_3S_4. Increase of S:Co up to 8:1 (a value limited by solubility of sulfur in DCB) did *not* result in the formation of a more sulfur-rich phase, such as CoS_2. Using S:Co values falling between two values corresponding to one-phase compositions (in this case, falling between two of S:Co = 0, 8:9 or 4:3) leads to a mixture of the two expected phases. Thus, one can say that the sulfidation reaction is complete within 15 seconds at 182°C. One interesting aspect of the data is the persistence of peaks of the 'minority' phase almost right up to the S:Co value required for complete disappearance of the minority phase. This suggests that sizeable ($>$ 1 nm) crystalline domains with peaks sufficiently sharp to be distinguishable from the instrumental background are present in samples which contain almost enough sulfur for consumption of the minority phase. This will be considered again in the next chapter.

The information in XRD patterns was used to estimate the size of a single crystal domain in one-phase colloids of Co_3S_4 and Co_9S_8 nanocrystals. Theoretical XRD patterns were computed for both phases assuming various crystal size and shapes. As can be seen

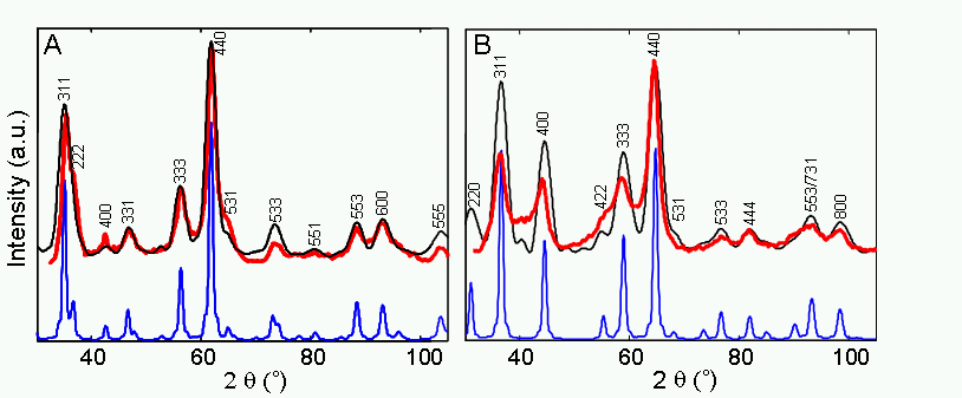

Figure 3.2: Experimental and theoretical XRD patterns for the nanocrystal powders of cobalt sulfide. Experimental patterns for powders of hollow nanocrystals are shown by the red curves; black curves are patterns simulated for cubic domains of 3-4 nm size and the blue curves are simulated patterns for single crystalline hollow shells of dimensions measured in TEM. (A) Patterns for Co_9S_8, (B) Patterns for Co_3S_4.

in Fig. 3.2, observed peak widths are too wide to match the case of single crystalline shells of the dimensions observed by TEM. In contrast, reasonable fits to the patterns in terms of matching the linewidths can be obtained by assuming cubic domains of edge length of 3-4 nm. The shell thickness also falls within this range of lengths, so an average shell viewed in cross-section is expected to contain a single grain along the radial direction and display several grains (∼4-6 using TEM measurements) strung along the circumference. The agreement between the patterns and the simulations is not perfect for Co_3S_4: some experimental peaks (e.g. {422}) are broadened to a greater extent than average and some peaks appear stronger (e.g. {400}) or weaker (e.g. {422}) than expected. In general, a combination of anisotropic average grain shape, presence of stacking faults and non-negligibly broad grain size distribution may need to be considered in simulations to improve the agreement between simulation and theory.

3.1.2 Morphology

High-resolution TEM (HRTEM) observations agree very well with the interpretation of the XRD data. A relatively small fraction of the sulfide shells are oriented correctly

on the substrate for imaging of lattice planes, limiting the statistical significance of conclusions drawn from the data. However, the majority of shells observed with HRTEM were indeed polycrystalline, containing a small number of grains strung along the shell circumference (Fig. 3.3A&B). Some apparently single-crystalline shells were also observed, but were relatively rare. These descriptions apply to HRTEM images obtained from both Co_3S_4 and Co_9S_8. The grains observed did not seem to display any noticeable epitaxial relationship to each other. The defect structure of the shells, including grains boundaries, and possibly cracks and pores, is significant for applications in chemical control: small molecules may diffuse into hollow shells through such defects, as was suggested by catalytic activity of Pt particles embedded in CoO shells prepared by use of the Kirkendall-type process described here.[21] We also note in passing that some types of crystalline defects in minerals, at least in bulk structures, have been argued to provide stereochemically constrained environments for organic molecule assembly.[60] While the sulfide shells seem to be stable in DCB, they have a noticeably greater propensity to precipitate in comparison to Co nanocrystals. For example, sulfide shells, once precipitated from DCB by addition of methanol and centrifugation are difficult to redissolve. It appears that oleic acid and/or TOPO continue to bind to particle surfaces following sulfidation of the particles, but they bind less strongly to the sulfide particles than they do to the metallic particles. The propensity of nanocrystals to self-assemble into ordered aggregates also decreases, but does not vanish upon sulfidation: Fig. 3.3C shows a sample where evaporation of DCB left ordered aggregates on the grid. In comparison to $\epsilon-$Co nanocrystals, sulfide shells should experience much weaker attractive forces between each other due to weak polarizability and absence of magnetic interactions.

The occurrence of a moderate degree of ordering in aggregates suggests that relatively uniform dimensions of the shells are achieved, at least in some cases (in Fig. 3.3C, smaller solid particles are also seen alongside hollow relatively monodisperse particles). For use of such hollow structures in fundamental studies or in applications such as catalysis, the geometry and uniformity of the shells will likely need to be controlled. Thus, we performed

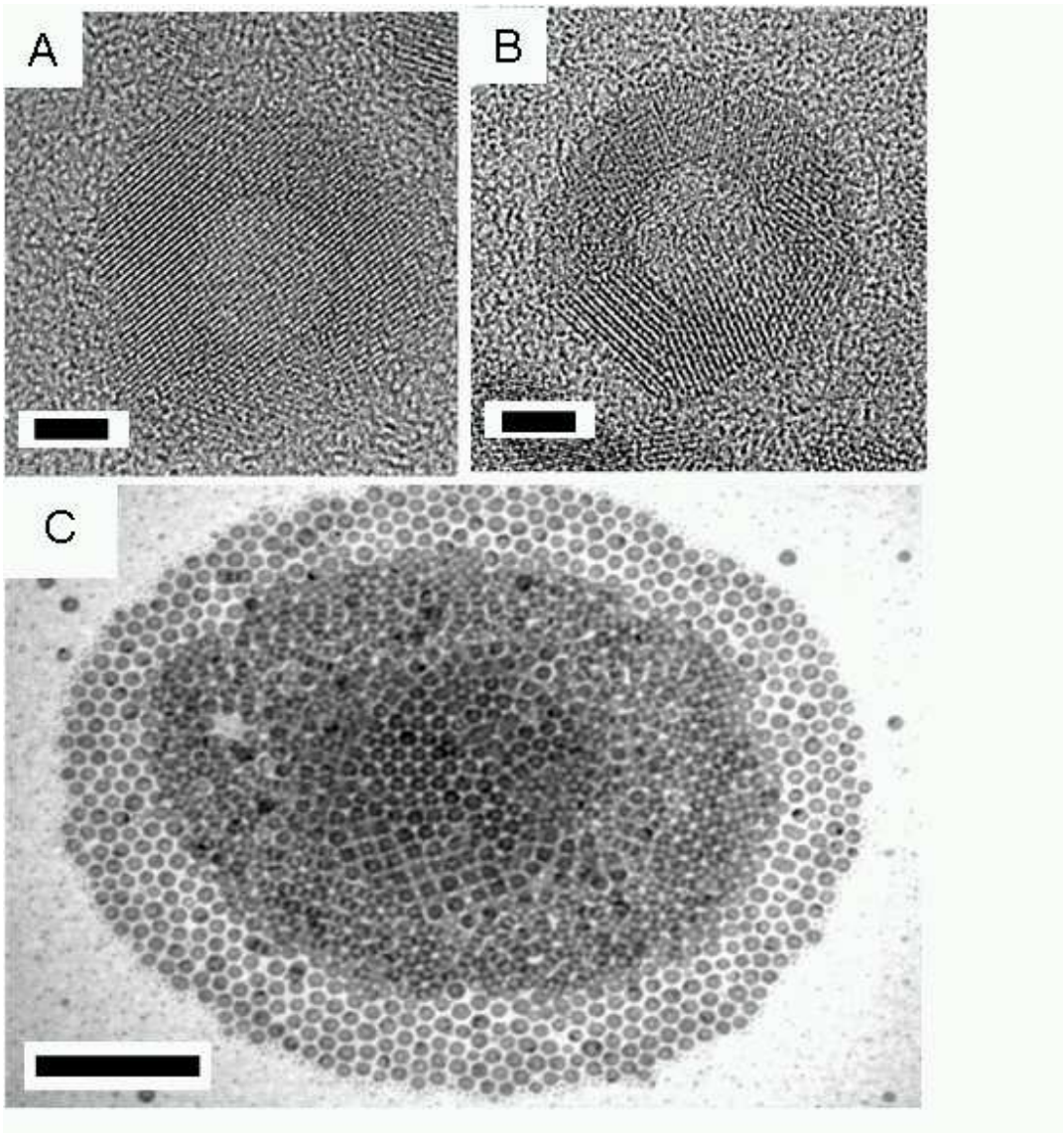

Figure 3.3: (A) HRTEM of sulfide shell with one large crystalline grain evident (B) HRTEM of sulfide shell with 4-6 crystal grains visible. Such multicrystalline grains are predominant for both Co_3S_4 and Co_9S_8 preparations. Scale bars: 3 nm. (C) Hollow particles also aggregate into packed structures, but due to weaker forces or broader size distributions, the degree and spatial range of translational order in the aggregates is not as strong as in aggregates of monodisperse $\epsilon-$Co nanocrystals.

measurements on TEM images to characterize the shape of the final products. Some small solid particles were seen in the sulfide sample; at this point, they can be assumed to arise from sulfidation of small, low-contrast Co nanocrystals that may be present in the starting colloidal solutions. Thus, these particles are not counted in the statistics. The outer diameter (OD) and inner diameter (ID) of each particle was measured. Diameters, D, of the starting cobalt nanocrystals were measured as well. Fig. 3.4 shows one set of such measurements. Qualitatively, the standard deviation of the particle size distribution does not seem to broaden much upon sulfidation. Expressed in fractional terms, however, the standard deviation of the ID distribution is significantly larger than that for D. This might be attributed to strong sensitivity of ID to total volume of material inflow during shell growth. Such an effect was seen in numerical models of the growth of multiphase shells on micron-scale particles,[61] where the inward growth velocity of a spherical front goes through a minimum and then accelerates to the spherical geometry. It is important to note that the average for the void diameter, μ_{ID} is only $\sim$60% of μ_D, the average starting Co particle diameter. Apparently, inward relaxation or growth of the inner shell wall by $\sim$2.5 nm occurs during the formation of a shell. Outward growth from the original Co-solution interface is, in comparison $\sim$3.5 nm. This is in contrast for findings for growth of thick sulfide films where inward advance of the cobalt-sulfide interface is completely negligible in comparison to outward advance of the sulfide film into the vapor region.[62]

Using the set of corresponding ID and OD values, shell volume for each measured particle and thus the volume distribution of shells was estimated. In Fig. 3.5, this distribution is compared with the shell volume distribution expected based on the ideal volume increase upon sulfidation and size distribution of the starting Co particles. The higher-volume half of the shell volume distribution can match the expected distribution only after assuming shells to possess 25% more volume than expected upon sulfidation. For shells with the smallest volumes, no obvious deviation from the ideal one calculated from the Co nanosphere diameter distribution is observed. Volume calculations based on TEM mea-

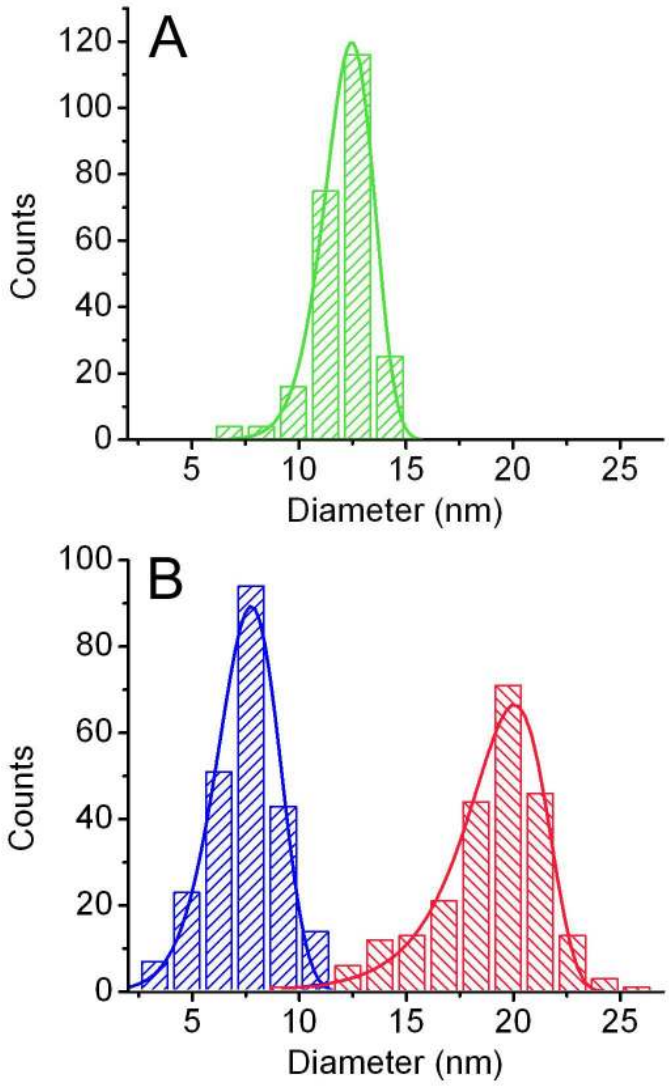

Figure 3.4: (A) Diameter distribution for as-synthesized solution of $\epsilon-$Co nanocrystals; ($\mu = 12$ nm, $\sigma = 11\%$), (B) Size distribution for hollow sulfide shells produced using the nanocrystals in A. The blue curve is the distribution of inner diameters ($\mu = 7.5$ nm, $\sigma = 21\%$). The red curve shows the outer diameter distribution ($\mu = 19.5$ nm, $\sigma = 13\%$).

surements should have an error of ∼15% under ideal circumstances, but may reach ∼30% if simply the magnification reported by the instrument is used to calibrate distances in images.[63] We attempted to minimize errors in magnification calibration: a constant magnification was used, a standard procedure for setting stage height was followed, collection of all images within the same day avoided large changes in instrumental parameters between measurements. On the other hand, a procedure commonly required for very reproducible length measurements, setting of objective lens currents to a constant value and manipulating stage height to focus on particles had to be omitted, as it proved too time-consuming for collection of statistics. Thus, the individual error in volume values should lie somewhere between 15% and 30%, presumably closer to the lower end of the range. Calculation of porous volume fraction is insensitive to systematic instrument calibration errors as the same magnification was used throughout. Furthermore, errors due to variation of lens currents should partially cancel when many measurements are combined, as done in the construction of the volume distributions. Also, several other, less comprehensive sets of data have *all* yielded positive deviation (5%-40%) from shell volumes expected from ideal sulfidation of starting Co particles of measured volume distribution. Thus, the data suggest strongly that ∼20% of the volume of an average sulfide nanoshell takes the form of pores, voids, cracks etc.

3.2 Mechanism: Kirkendall-Type Effect

Cobalt is the major component in one class of superalloys used to construct parts, such as turbine blades, that need to withstand elevated temperatures and aggressive chemical environments. Thus, sulfidation of bulk cobalt has been studied in some depth, with a particularly impressive set of experiments by Mrowec and colleagues.[62,64–67] It was demonstrated convincingly that growth of μm or mm-scale sulfide films on bulk cobalt proceed almost completely by outward transport of Co cations from the buried Co to the sulfide-vapor interface. Thus, it is reasonable to postulate that hollow particles are formed due to

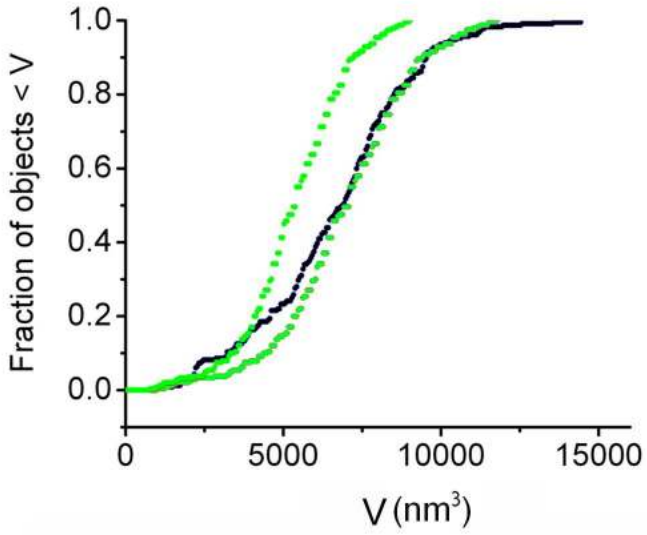

Figure 3.5: The blue curve is the cumulative volume distribution for sulfide shells calculated from TEM measurements. The green curves, on the left and right, were obtained by scaling up the calculated volumes of starting $\epsilon-$Co nanospheres by a factor of 2.9 and 3.8 respectively. The ideal ratio of final to initial volume for the sulfidation reaction is 3.06.

outward cobalt transport through the growing sulfide shell dominating over inward transport of sulfur atoms/anions. While no clear evidence for formation of voids or pores was presented in the bulk sulfidation studies, pore formation in metallic specimens upon oxidation is well-known and understood to result from negligible diffusion of anionic species during growth. In comparison to such microstructures seen in bulk, the sulfide nanoshells display dramatically more obvious porosity. An explanation of this difference is warranted.

Void formation as a result of directional diffusion has been considered quite extensively in the conceptually related area of metal-metal interdiffusion. Smigelskas and Kirkendall demonstrated, for the first time in 1947, that diffusive processes operating in a couple formed by joining of two compositionally different specimens result in net directional flow of matter.[22] The sample for this experiment was a block of brass coated with a pure copper layer. Brass, rather than pure zinc was chosen as the core material to eliminate effects due to volume change upon mixing. At elevated temperatures, the brass-copper interface was observed to migrate inwards. The shrinkage of the central block as a function

of time could be understood within diffusional kinetics and metallography confirmed that outward diffusion of zinc into copper is faster than inward diffusion of copper into brass. These unequal matter flows could not be understood within the then-dominant picture of solid-state diffusion proceeding by atom exchange between lattice sites. Thus, the experimental results, commonly summarized under the term Kirkendall Effect, provided the first experimental evidence for vacancy-mediated hopping of atoms being the most important diffusive transport mechanism in crystals.[68]

Formally, a directional flow of matter in crystalline matter is accompanied by an opposing flow of vacancies. This picture provides a natural explanation for common observation of porosity accompanying the Kirkendall Effect. Vacancy concentration builds up on the fast-diffusing side of the couple; when the vacancy concentration exceeds the saturation value, voids are nucleated by condensation of vacancies. Shrinking of one side of the diffusion couple may be attributed to generation and motion of dislocations under stress fields generated by an increasing vacancy concentration. Motion of dislocations, sustaining plastic deformation, consumes vacancies. Thus, void formation and deformation are competing processes resulting from removal of material from the fast-diffusing side. Furthermore, even typical dislocation densities observed in undeformed metals have been argued to intercept a sufficient fraction of vacancy flux such that void formation is suppressed or delayed significantly.[69] On the other hand, porosity upon oxidation may become more pronounced for samples with a high surface-to-volume ratio and greater crystalline perfection, e.g. thin films, due to confinement of vacancies into smaller volumes, and a relative enhancement of vacancy injection rate.[70] Attainment of very pronounced porosity in sulfide nanoshells may thus be attributed to further increase of surface-to-volume ratio and crystalline perfection when the starting materials are in the form of colloidal nanocrystals.

The term ‘Kirkendall Effect’ has been used most commonly in the area of interdiffusion in couples composed of alloys. However, the possibility of compound formation is not excluded in its usage, most commonly in the case of formation of intermetallic compounds

at interfaces accompanied by diffusional flow. It seems that the term is not used as widely in the field of metal oxidation. Perhaps, this is because absolutely negligible diffusion of anionic species is not uncommon in metal oxidation, leading to recognition of void formation due to outflow of cations before Kirkendall's experiments were undertaken. We believe that in-solution alloying (*or* dealloying) reactions performed on metallic nanostructures will also produce hollow nanostructures through the same mechanism; thus, we will somewhat cautiously label the general diffusional phenomenon we hypothesize to produce the observed hollow nanostructures a *Kirkendall-type* process.

3.3 Related Systems

In bulk systems, void formation as a result of oxidation or the Kirkendall Effect has been treated largely as an issue of theoretical interest or in the context of reliability of solders, joints etc. where microstructural changes upon reaction or interdiffusion may prove detrimental to the integrity or performance at the junctions. We were able to locate only one prior experimental study where a Kirkendall-type process was used deliberately to create a highly porous material: Aldinger showed that a compacted powder of Be-coated Ni microparticles ($\sim 30\mu m$) will transform at T $> 900^{\circ}$C and over 5-6 hours into an aggregated, porous material consisting of roughly spherical 'cells'.[71] Due to fusing of adjacent particles, a quite heterogenous arrangement of pores is seen to develop in images of cross-sections of the sample. In comparison, by isolating void condensation into single nanocrystals, we have obtained the simple scenario of one spherical void per particle. On the other, the void volume fraction seems larger in images presented by Aldinger.* Emergence of porosity in the microparticle compact follows quite a characteristic path. In particular, at intermediate

*In fact, the numerical values reported for the volume change upon interdiffusion of Be and Ni reach as high as 250%. It is difficult to see how a diffusional process operating in a spherical core-shell geometry can yield a value larger than 100%. Aldinger explained his results semi-quantitatively by hypothesizing outward *stretching* rather than outward deformation of the shell as the core material is added to it. The physical basis for such a process is not clear although it seems to be required to explain Aldinger's data.

stages of the process, gaps begin to develop between a partially consumed core and the alloyed shell. As the reaction proceeds further, the core and the shell are connected by thinner and fewer filaments of material, eventually resulting in the complete consumption of the core material and the filaments.

Sulfidation of cobalt nanocrystals occurs too rapidly at 182°C for monitoring of the void formation process by TEM imaging of aliquots collected from the reaction mixture. It was found that by placing Co nanocrystals into a suspension of fine selenium powder in DCB at 182°C leads to formation of hollow CoSe particles. In this case, it *is* possible to catch particles at different stages of the selenization reaction. The images obtained seem to display essentially the same stages as observed by Aldinger (Fig. 3.6). The similar geometrical evolution of the two systems supports a Kirkendall-type mechanism driving the formation of hollow nanoshells. The emergence of filaments connecting the core and the growing shell may be attributed to preferential nucleation of voids near the core-shell interface: vacancy concentrations build up first in that region and the interfacial energy lowers the activation energy for void nucleation. (Aldinger argued that stress build-up due to increased vacancy concentration would result in fracture at the core-shell interface. In the case of our hollow nanocrystals, confinement of the reaction into length and timescales compressed by at least 3 orders of magnitude may blur the distinctions between processes such as fracture, delamination or void nucleation.)

As will be described in detail in the next chapter, lowering the sulfidation temperature down to 120°C slows the reaction, but not sufficiently for monitoring of reaction kinetics: the reaction at 120°C completes within minutes and the uncertainty in collection time due to cooling of solution, manual collection of aliquots etc. are large enough to confound quantitative studies. Lowering of the sulfidation temperature below 120°C leads to inhomogeneous morphologies and the reaction rate varying strongly between syntheses performed at apparently the same conditions. Reproducible behavior is recovered once again when the sulfidation temperature is lowered even further to room temperature; however,

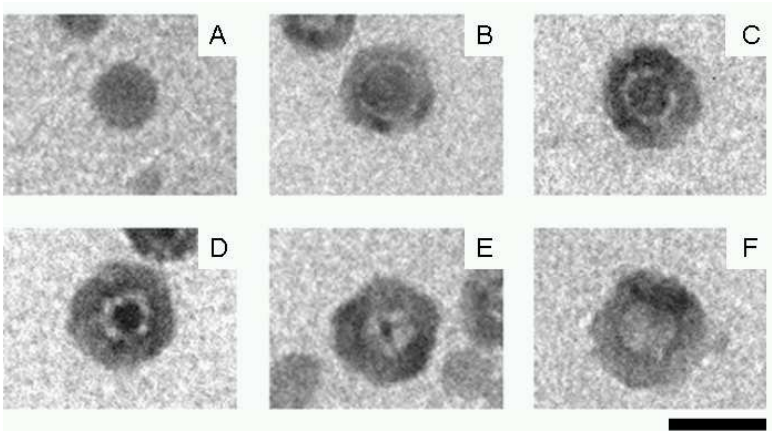

Figure 3.6: Nanostructures formed upon addition of Se suspended in DCB onto a colloidal solution of Co nanocrystals. The images are for particles observed (A) before addition of Se and (B) 10, (C) 20, (D) 60, (E) 120, (F) 1800 seconds following addition of Se. Note that particles within the same images are sometimes at very different stages of the selenization process. Continual dissolution of suspended Se particles into DCB may be argued to result in local Se concentration variations and lead to the observed heterogeneity in the reaction rate. (© American Association for Advancement of Science)

in this case, the morphological evolution follows a path that is difficult to trace with TEM imaging. By locating a synthetic system where the reaction rate varies more predictably with temperature, it should be possible to estimate activation energies and better determine the nature of the rate-limiting process at different temperatures, reactant concentrations etc.

Some reports of formation of hollow nanostructures upon oxidation exist in the literature and merit mention. Catalytic Cu particles on a MgO support have been seen to transform first into hollow structures and finally into ring-shaped structures upon exposure to oxygen.[72] Wetting of the substrate by the metal and metal oxide provide the necessary symmetry breaking for the eventual formation of a ring, rather than a shell. Void formation was explained in this case by invoking not solid-state cationic diffusion, but extrusion of molten metal through gaps in the oxide shell. The heat of reaction upon oxidation was argued to provide the energy necessary to heat the Cu core to a significant fraction of its melting point, T_M^{Cu}. Under the assumption of no heat loss into the surroundings, heat

evolved upon formation of ≥2 monolayers of oxide was shown to be sufficient to induce near-melting ($T > 0.5\ T_M^{Cu}$) in this case. Thus, in general, this mechanism merits consideration alongside Kirkendall-like processes when hollowing of nanostructures accompanies their chemical modification. In the next chapter, we will see that hollow shells may be obtained under conditions where the sulfidation reaction takes ≥60 seconds to complete. For sulfidation of colloidal cobalt in solution, when complete sulfidation requires a measurable long interval, the rise in nanocrystal temperature is expected to be <1 K based on an order of magnitude estimate.* Thus, a Kirkendall-like process provides a more likely explanation of our results. At the very beginning of the reaction, diffusional/electrical barriers to sulfidation are minimal and the reaction proceeds most rapidly. It is possible that a significant, but transient rise in temperature of the particle occurs at this stage. This possibility seems intimately connected to the idea of a reaction zone in a solid-state transformation, where interface relaxations and heat released upon reaction modify reaction dynamics and pathways.[59]

Formation of *free-standing* hollow nano- or microstructures of metal oxides has also been reported; however, the observations we were able to locate were either presented without discussion of the formation mechanism[75,76] or were explained within a multi-step material- or chemistry-specific mode of growth,[77–79] rather than being attributed mainly to a diffusional process. We believe that a Kirkendall-type process operating on an initially metallic particle is involved in most, if not all, of these cases of the formation of

*Heat flux through the solvent, rather than the sulfide shell limits heat transport away from the nanocrystal due to the much lower thermal conductivity of solvent and negligible thickness of the shell in comparison to amount of solvent per nanocrystal. If a spherical object is maintained at an elevated temperature, higher than the temperature of the surrounding medium by ΔT, heat flux into the medium is $k\Delta T R^{-1}$, where k > 0.01 $W \cdot m^{-1}K^{-1}$ for most organic solvents[73] and R, particle radius, varies between 5-10 nm during sulfidation, giving a flux of $[10^7\ W \cdot m^{-2}K^{-1}][\Delta T]$. Total heat released by sulfidation of a 10 nm thick cobalt film into Co_3S_4 can be estimated to be 200 J/m^2 using thermochemical data.[74] Taking the ratio of the two quantities, we find that heat dissipation into the solvent equals heat generation when $(t \times \Delta T) \sim 10^{-4}$ sec$\cdot K$, where t is the time for completion of the reaction. Thus, for a reaction that takes >0.1 seconds to complete, the rough estimate for the temperature rise is 0.001 K. It is probably not well-justified to use parameters for bulk materials and we have not considered flow of heat into the metallic core. However, the extremely small temperature rise predicted suggests that heat transport away from the particle is sufficient for the metal core to remain solid throughout the reaction.

hollow nanostructures. The formation of Au nanoboxes using Ag nanocrystals as starting materials[78] using the transmetalation reaction,

$$\mathrm{Au}^{3+}_{(aq)} + 3\mathrm{Ag}_{(s)} \longrightarrow Au_{(s)} + 3\mathrm{Ag}^{+}_{(aq)}$$

may reasonably be attributed to the removal of three atoms from the silver 'core' upon deposition of a single Au onto a gold 'shell'. However, even in this case where the two components are chemically very similar, the slightly smaller size of the Ag^+ cation (r $\sim$ 1.2 Å) in comparison to Au^0 (r $\sim$ 1.46 Å) suggests that a Kirkendall-like process may additionally be involved in the formation of these structures.

3.4 Kirkendall Void Formation in a Spherical Geometry

It is useful to construct an idealized model of hollowing of a spherical nanostructure due to a Kirkendall-type process. There are several interesting questions that analytical or numerical models could address: Are deviations from thick-film behavior due to the 'closed' topology or to a change in physical growth mechanisms as particle size shrinks? What value must the dimensionless parameter D_A/D_B (where D_A and D_B are the diffusivity, through compound A_mB_n, of respectively the core species A and the dissolved species B) exceed for formation of hollow nanostructures? etc.

Different theoretical approaches are likely to have different strengths and weaknesses, as the actual process is potentially complex, involving material parameters relating to electrical field gradients, free energy as a function of composition and defect content, strength and anisotropy of stress fields around vacancies and voids etc. A moving boundary formulation taking into account time-dependent diffusion equations can determine evolution of local composition and the time required for void nucleation;[80] however, it cannot address formation of voids and their impact on further progress of the reaction. Alternatively, Monte Carlo simulations may be used to evaluate the validity of different macroscopic treatments of diffusion under different assumptions about lattice deformation and

vacancy generation/annihilation.[81] Such approaches can probably address general features of Kirkendall-type processes in simpler cases of interdiffusion in alloys. For more strongly driven processes, where multiple phases and a complex defect structure may be present, such as the formation of sulfide nanoshells described here, application of phase-field[82] or molecular dynamics[83] methodology will likely be required to address the interplay between morphology, diffusion, defect structure and local chemical composition. Unfortunately, such models may require input of a large number of materials parameters, addressing one specific system at a time until general classes of behavior emerge.

Here, we derive very general minimal conditions for use of Kirkendall-type processes in making hollow structures from solid starting materials. Specifically, we consider the implications of competing inward and outward diffusion-limited growth within a spherical geometry. Depending on the specific materials and defect chemistry, this picture may or may not provide a correct view of shell growth. One very possible alternative to this mode of growth would be reaction-limited, rather than diffusion-limited, advance of the shell in one direction. This might be the case, for example, if the shell can keep growing inward despite local deficiency of the dissolved species at the core-shell interface, e.g. if the shell material accommodates a significant amount of anionic vacancies. Many other simplifying assumptions are involved. (We neglect, among other things: electric-field driven transport and non-linear diffusion that can operate in thin films, possible presence of fast-diffusion paths such as grain boundaries, build-up of stress either in the shell or core and the contribution of interfacial energies to the overall driving force for transformation. Many of these assumptions become more reasonable as thicker shells are considered and upon choice of atomically smaller, faster-diffusing cationic species for the core material; the exception is growth stresses which will tend to increase with the mismatch between anion and cation size or with increasing shell thickness. As most of the assumptions we make favor, rather than oppose, void formation, the derivation essentially refers to necessary, not necessarily sufficient, conditions for synthesis of hollow structures.). However, it should still be

possible to create synthetic conditions where our assumptions provide a reasonable first approximation.

The derivation proceeds by considering growth of a spherical shell of composition A_mB_n around a completely deformable core material (see Fig. 3.7 for a summary of the terms). The core material is assumed to stay in contact with the shell throughout growth and not oppose inward growth of the shell in any way. We consider that the core species, A, may diffuse outward to the shell-solution interface and react with molecules of the dissolved species B impinging on the solid particle. Similarly, inward diffusion of B atoms/ions gives rise to inward growth of the shell by consumption of the core. Choosing our units such that the initial particle radius $r_0 = 1$ simplifies the mathematics considerably. Assuming steady-state diffusion concentration profiles, we find the magnitude of the flux of species i, J_i, as a function of the radial coordinate, r,

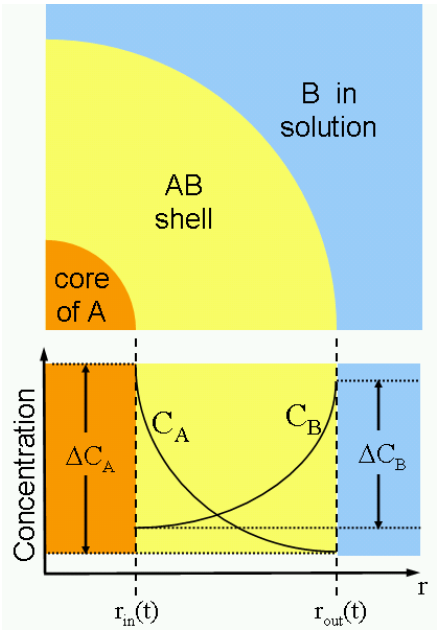

Figure 3.7: Description of the geometry considered for the derivation in the text.

$$|J_i| = \frac{D_i \Delta C_i}{r^2} \times \frac{r_{in}(t) \cdot r_{out}(t)}{r_{out}(t) - r_{in}(t)}, \tag{3.1}$$

where $r_{in}(t)$ and $r_{out}(t)$ refer to the positions along the radial coordinates respectively of the core-shell and shell-solution interfaces. Note that ΔC_i refers to the change in concentration of species i across the shell and that we have assumed diffusivities D_i to be independent of the local composition given by C_i. Rates of growth in the two directions should respectively be proportional to J_A and J_B, so we have,

$$\frac{dr_{out}}{dt} = |J_A(r_{in}(t), r_{out}(t))| \cdot \frac{v_{AB}}{m} \tag{3.2}$$

$$\frac{dr_{in}}{dt} = -|J_B(r_{in}(t), r_{out}(t))| \cdot \frac{v_{AB}}{n} \tag{3.3}$$

$$r_{in} \quad = \quad r_{out} = 1, \text{ for } t = 0, \tag{3.4}$$

a very simple system of two 1^{st} order differential equations describing the coupled evolution of r_{in} and r_{out} as a function of time. v_{AB} refers to the molar volume of the product A_mB_n These equations may be solved numerically for different values of D_i and ΔC_i.* One such solution is shown in Fig. 3.8. Note that there is nothing in the formulation to determine when shell growth ends; the system of equations evolves until $r_{in} = 0$ without regard to whether the amount of material formed is less than or greater than the actual amount of material that will be formed given the original size of the core. In reality, mass balance needs to be imposed to determine the time, t_{fin}, at which reaction has completed. This is accomplished by inspecting the solutions and picking the time at which the volume of the shell matches the volume expected based on the volume of the initial material, i.e.

$$r_{out}^3(t_{fin}) - r_{in}^3(t_{fin}) = 1 + \Delta v \tag{3.5}$$

where $\Delta v = (v_{AB} - v_A)/v_A$ with v_{AB} and v_A the molar volumes of the shell and core materials. This expression applies for units where $r_0 = 1$.

Equations 3.2-3.4 are simple enough that an algebraic solution for the final geometry may be found. The ratio of the inward and outward growth rates (using Eqn. 3.1 for i = A,B and Eqn.s 3.2 & 3.3) possesses a simple form as a function of time

$$\frac{\frac{dr_{out}}{dt}}{\frac{dr_{in}}{dt}} = \frac{mD_A\Delta C_A}{nD_B\Delta C_B} \times \left|\frac{r_{in}(t)}{r_{out}(t)}\right|^2 .$$

The time infinitesimals on the left hand side may be canceled to yield a single differential equation relating $r_{out}(t)$ and $r_{in}(t)$. Solving this equation and imposing initial conditions yields an algebraic expression satisfied throughout shell growth:

$$K \cdot r_{out}(t)^3 + r_{in}(t)^3 = 1 + K \tag{3.6}$$

where $K = (mD_A\Delta C_A)/(nD_B\Delta C_B)$. Simultaneous solution of this equation (with $t = t_{fin}$) and the mass balance condition, Eqn. 3.5, gives the ratio of final void diameter to final

*$J_i \to \infty$ as $t \to 0$ since $r_{in}(t_0) = r_{out}(t_0)$. Setting $r_{in}(t_0) = 1 - \epsilon$ & $r_{out}(t_0) = 1 + \epsilon$, where $\epsilon << 1$, one obtains numerical solutions insensitive to magnitude of ϵ. In a physical picture, this is equivalent to allowing for instant formation of a *very* thin shell. In any case, numerical solutions are used only for demonstration of the validity of a simple analytical treatment, so numerical error is not an important consideration for what follows. We also note here that an algebraic solution also seems possible, but yields rather cumbersome expressions.

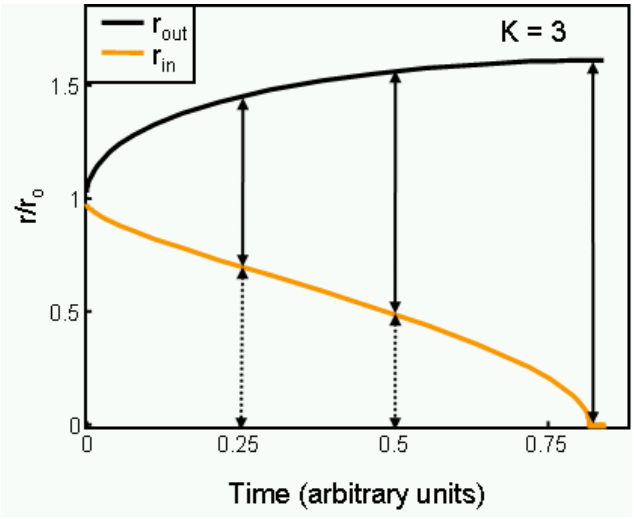

Figure 3.8: Numerical solution of equations for a specific combination of parameters D_i and ΔC_i. K, set to 3.0 in this example, is a dimensionless combination of these parameters. Positions of inner and outer shell interfaces normalized by initial solid particle radius, r_0, are plotted. Thin and thick vertical arrows show respectively core radius and shell thickness at a given time. Final geometry is determined by picking the time where calculated shell volume indicates complete consumption of core material.

outer diameter,

$$\frac{ID}{OD} = \frac{r_{in}(t_{fin})}{r_{out}(t_{fin})} = \left[\frac{1 - K\Delta v}{2 + K + \Delta v}\right]^{1/3}, \tag{3.7}$$

Interestingly, a negative void diameter is predicted by this expression when $K \times \Delta v > 1$. In the picture of Fig. 3.8, this corresponds to choosing Δv sufficiently high that at the time that the core has shrunk to a diameter of zero, the shell volume is still less than the value corresponding to complete consumption of core. Formally, the core has shrunk to a diameter of zero with a finite amount of unreacted material remaining in it. The original assumption of unopposed inward growth of shell is thus not physically valid for the combination of fast inward growth and large volume increase upon reaction. Thus,

$$\frac{mD_B\Delta C_B}{nD_A\Delta C_A} > \Delta v \tag{3.8}$$

is one minimal condition for growth of hollow spherical structures. When it is violated, the core material is not transported outwards sufficiently quickly for creation of space for

diffusionally-favored inward shell growth. Stress will build up at the core-shell interface, leading to an overall transformation rate limited by outward transport of the core material, potentially leading to passivation. If the driving force for reaction is large and cohesion at interface weak, cyclic cracking and regrowth of a thin shell could result, leading to formation of many small, solid particles.

Even when expression 3.8 is satisfied, an additional condition on shell growth can be envisioned. The hollow shell must remain stable throughout the time that it is held at the synthesis temperature. Derouane argued that a simple guideline for stability of hollow structures against collapse into a ring structure on a substrate is that $T < 0.5T_M^{AB}$ where T is the 'synthesis' temperature and T_M^{AB} is the melting point for the shell material. For most colloidal preparations, we expect $T < 0.5T_M^{AB}$ such that lattice diffusion, not bulk flow, will dictate the stability of the shell. Recently, it was shown by Gösele and Tu that the void in a hollow nanostructure will 'evaporate' through outward diffusion so as to minimize total surface energy. The timescale for complete removal of the void in a single-component spherical shell was estimated to be,

$$t_{shrink} \approx \frac{l^3 kT}{10\gamma D\Omega}, \tag{3.9}$$

with l, γ and Ω denoting respectively, the void diameter, interfacial energy associated with inner and outer surfaces and the volume of a vacancy. D refers to the diffusivity of the shell material. In the case of a binary compound, as long as segregation of the two components is unfavorable, the effective diffusion constant for shrinking of the void will be dominated by D_B, the diffusivity of the slower species. In comparison, our numerical solutions confirm that for $D_B << D_A$, the time for the formation of a hollow shell is,

$$t_{synth} \approx \frac{d^2(1+\Delta v)^{2/3}}{6D_A\Delta C_A}, \tag{3.10}$$

where d is the diameter of the starting particle. We expect that 3.8 is satisfied comfortably, so that $l \sim d$. Note that time for void elimination depends more strongly on particle/void

size than time required for growth of the shell, presumably due to the surface-energy driven nature of the void evaporation process. Assuming that a reaction is quenched instantly following completion of shell formation, stability of the shell requires that $t_{shrink} > t_{synth}$, i.e.,

$$\frac{D_A \Delta C_A}{D_B} > \frac{2\gamma\Omega}{kTd}. \tag{3.11}$$

Using numbers reasonable for our hollow cobalt sulfide shells*, this condition is very roughly, $D_A/D_B > (4\Delta C_A)^{-1}$. Note that ΔC_A is necessarily less than unity and its magnitude essentially measures the compositional variation across the shell created by presence of the two reactant species on the two sides of the shell. As we do not know the magnitude of ΔC_A, it is not possible to guess whether transport (Eqn. 3.8) or stability against collapse at synthesis temperature (Eqn. 3.11) presents the more stringent conditions for the sulfide nanoshells. However, it is interesting to note that stability of voids against collapse becomes the limiting condition for synthesis of hollow shells for $\Delta C_A < 0.125$, not an unlikely condition given the ionic nature of the shell material.

3.5 Summary & Generalizability of Method

The data presented in this chapter illustrate a process that is most naturally explained through a Kirkendall-type effect. In most ionic or mixed ionic-covalent crystals, cation mobilities are significantly higher than anion mobilities. Thus, the formation of cobalt sulfide shells presented here should immediately generalize towards synthesis of hollow shells of many materials. The most immediate extension would be use of nanocrystals of different transition metals as the core material and use of different molecular species as the oxidizing species. This approach has indeed recently been shown to modify morphology of starting metallic nano- and microstructures with the final product composition spanning CdS,[84] CoO,[21,85] PbS[27] and ZnO.[86] In principle, alloying and transmetalation reactions may also

*$\gamma = 2\ J/m^2,\ T_{synth} = 450\ K, \Omega_{Co^{2+}} \sim (1.5\mathring{A})^3, d = 9nm$. The value for γ is conservative in that it is chosen from the high end of the range typical for ceramic-vapor interfaces.

involve reactants of significantly different mobilities; thus, formation of hollow metallic or alloyed structures may also be anticipated. The driving forces for these reactions may not be as large as for binary-compound formation. In the simplified language of the discussion in the previous section, ΔC_A is smaller for these reactions, making it more difficult to produce a hollow structure much faster than it is destroyed by void evaporation. On the other hand, volume increase, Δv will tend to be smaller for alloys and intermetallics, making it easier to satisfy 3.8. In fact for the transmetalation process described by Sun and Xia,[78] it may make some sense to assign a negative number for the relative volume increase.

It is notable that TEM images show the inner wall of the sulfide shell to be located $\sim$2 nm from the initial core-solution interface position. Whether this is due to the formation of a reaction layer, to partial void collapse before reaction can be quenched or to a nanoscale analogue of deformations seen in bulk Kirkendall experiments is not clear. Whatever the explanation, it seems that it should not be possible to realize a void in sulfide particle with diameter <4nm without a significant change to the recipe used. A lower limit of similar magnitude may apply for other shell compositions. Evidence for some porosity or roughness in the shells was also presented.

While extension of the methodology to different material systems of interest is clearly a worthwhile undertaking, it is also justified to study some specific systems in greater detail in terms of the mechanism of the hollowing process. The next chapter presents some further exploration of the cobalt sulfide nanoshell synthesis. By varying synthesis conditions and examining particle morphology, some further features of the transformation are uncovered.

Chapter 4

Details of the Sulfidation of Co Nanoparticles

Morphologies of hollow nanostructures obtained by chemical modification of metallic nanocrystals are much simpler in comparison to any structures observed in analogous bulk systems. This fact motivates 'mechanistic' studies of the evolution of such nanostructures. Ideally, chemical *and* morphological features of nanoparticles would be studied as they were being transformed. Diffusional kinetics have already been demonstrated to operate during oxidation of *solid* Fe_3O_4 nanoparticles into solid Fe_2O_3 particles. This study was facilitated by the existence of a near-IR absorption band characteristic of the starting material and a simple chemistry where the solvent also acts as the oxidizing agent.[58] We have not yet found synthetic conditions where chemical transformation can be monitored so unambiguously. Here, we focus instead on morphological evolution of hollow cobalt sulfide structures and its dependence on reaction conditions. Electron microscopy and x-ray diffraction are used to characterize the dependence of shape, crystallographic phases present and size distribution of particles on the synthesis temperature and synthesis time. Some trends connecting final product morphology to the reaction conditions and starting particle diameter emerge. The results support the picture of a vacancy-assisted diffusional

process. The data also provides evidence for processes accompanying shell growth which modify product morphology from one expected from a simple diffusion-based picture. Such deviations are likely to be generally involved in the production of hollow nanostructures based on the Kirkendall Effect.

4.1 Temperature Dependence of Morphology

The time required to form hollow particles decreases dramatically with the increase of temperature as may be expected. Furthermore, the morphological evolution of particles changes significantly in character over the temperature range between room temperature and 120°C in a way that demonstrates the diffusional processes at play. Fig. 4.1 shows TEM images of initial cobalt nanocrystals and their sulfides after reaction at room temperature (Fig. 4.1A), 120°C (Fig. 4.1B), and 182°C (Fig. 4.1C) respectively, with a sulfur-to-cobalt ratio of 4:3 used.

The reaction at room temperature is relatively slow. After 1 minute, a thin sulfide layer appears on the surface of the particles. The nanocrystal solution retains strong ferrofluidic behavior. Small voids are present between the cobalt core and sulfide shell, corresponding to vacancy condensation at the boundary. Cobalt cores disappear over time and are not easily distinguished by TEM after stirring at room temperature for 10 minutes. Small voids are dispersed within each nanocrystal such that there is not enough contrast to clearly reveal a porous structure. At this point, the sample shows a very weak ferrofluidic response to a $\sim$1 Tesla magnet. Gradual coalescence of small voids into bigger ones follows disappearance of visible Co cores. It takes $\sim$19 hours for the appearance of distinguishable hollow nanocrystals in TEM images. At this stage, most nanocrystals have voids inside them although it is still hard to resolve whether there is a single hole within each nanocrystal. These voids are not always located at the center of the spheres and possess quite irregular shapes. Complete consumption of Co can be verified by the absence of any

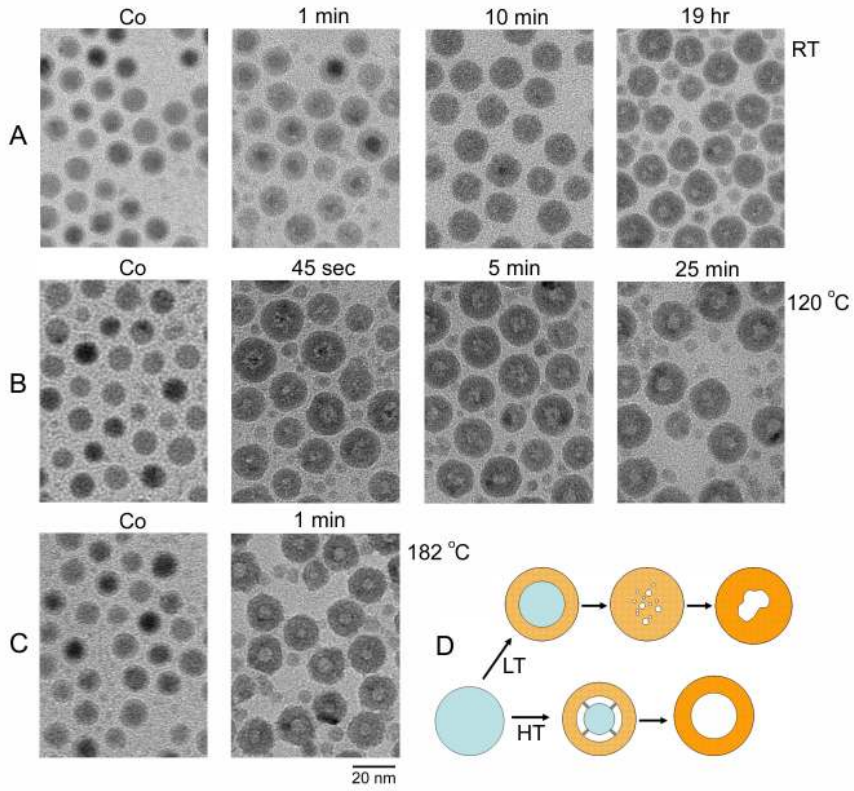

Figure 4.1: TEM images of nanocrystals originally metallic Co undergoing sulfidation (A) at room temperature (B) at 120°C (C) at 182°C (D) Schematic summary of low and high temperature growth modes. Time after commencement of sulfidation is indicated above each image.

ferrofluidic response of the solution to a magnet.

The reaction rate increases dramatically with increase of temperature. At 120°C, it takes only 45 seconds before an obvious empty gap develops between the core and shell (Fig. 4.1B). The cobalt core and sulfide shell are seen to be connected by filament-like bridges, resembling structures we previously observed during growth of a selenide shell on Co nanocrystals. These bridges may act as fast transport paths for the delivery of remaining Co onto the shell. Cobalt cores disappear quickly; within 5 minutes a single void with some remaining filaments in the center of the crystals is observed. These remains disappear as the reaction proceeds to completion, leading to hollow nanocrystals with distinguishable, regular, well-centered circular voids in most particles within 25 minutes. As mentioned in the previous chapter, at 182°C the reaction is too rapid for manual isolation of intermediate stages. The vast majority of nanocrystals formed at high temperature contain a single circular void located in the center of each particle (Fig. 4.1C). The two different modes of growth observed (for T$\geq$120°C and T$\sim$30°C) are schematically summarized in Fig. 4.1D.

Appearance of multiple voids within each particle upon lowering of the synthesis temperature to room temperature can be attributed to a decrease in vacancy mobilities. Thus, the core and the shell tend not to get separated by a clear gap as seen at higher temperatures. Instead, the shell grows inward incorporating many small voids. These voids coalesce given sufficient time, but since the cobalt core has been consumed before significant coalescence takes place, the tendency for the largest void to form at the center of the particle is visibly reduced. At intermediate temperatures, particles grow according to either mode, with the added complication that TEM images of particles obtained at intermediate reaction stages for reaction temperatures 70-100°C display some shells that look to be either partially fractured or on the verge of fracture (Fig. 4.2). Although there probably is not significant atom exchange between sulfide shells during synthesis, even at higher synthesis temperatures, small solid particles with diameter of a few nanometers are often present to a small extent in the product alongside hollow nanocrystals; these may

be fragments originating from fracture of growing shells. Thus, we believe that fracture processes occur, albeit less frequently, at higher temperatures as well, but currently have no hypothesis as to why intermediate temperatures should be most favorable for fracture.

As described in the previous chapter, the crystal phase of the product synthesized at high temperature is determined precisely by the molar ratio of cobalt and sulfur in the system. When the sulfur-to-cobalt ratio is less than 8:9 and the reaction is performed at 182°C, XRD analysis reveals the coexistence of Co_9S_8 and metallic Co in the final product. TEM inspections show the product to be a mixture of sulfide hollow spheres and solid Co particles. We conclude that the reaction at this temperature finishes before the sulfur solution can uniformly mix with the Co nanocrystal solution. When the reaction occurs with insufficient sulfur at a lower temperature (e.g. 120°C), the product is a uniform solution of core-shell particles as the reaction rate has been reduced below the time for compete mixing of the sulfur solution into the nanoparticle solution. When the sulfur-to-cobalt ratio is between 8:9 and 4:3, the product is a uniform solution of hollow spheres although XRD pattern shows that it is a mixture of both Co_9S_8 and Co_3S_4 phases. When the sulfur-to-cobalt ratio is greater than 4:3, the product is composed of single phase Co_3S_4 hollow nanocrystals. Incomplete mixing within the short reaction time at 182°C would also explain the persistence of detectably sharp peaks corresponding to the minority phase for Co:S ratios close to the value required for complete consumption of the minority phase.

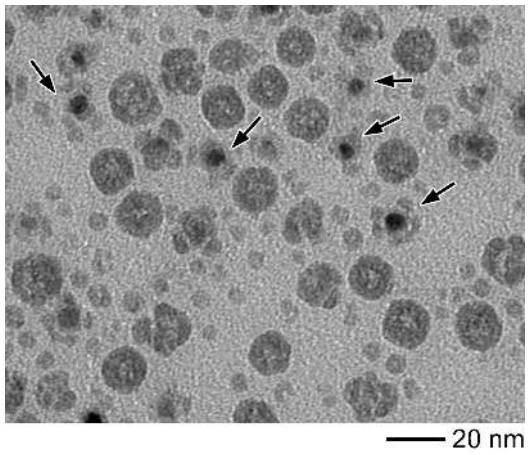

Figure 4.2: A sample obtained by sulfidation of $\epsilon-$Co nanospheres at 100°C. Arrows indicate highly defective shells which seem to have partially fractured or which seem to be on the verge of fracture.

4.2 Particle Shape & Statistics

Statistics on the size of hollow nanocrystals synthesized from cobalt particles at 182°C with sizes ranging from 9 nm to 14 nm were collected to check for dependence of final product morphology on the size of starting materials.

Relative void size is expressed as the average ratio between ID and OD providing a measure of the efficiency of the void formation process. The data is displayed in Fig. 4.3. The samples show mean ID/OD ratios in the range 30%-45%, smaller than 63%, the value corresponding to the idealized case of immobile sulfur atoms and a stationary Co-Co_3S_4 interface, giving another indication of inward growth or deformation of the shell during shell formation. The increase of the average value of ID/OD with average diameter of original Co nanocrystals in the range of our data suggests that inward growth of the shell mainly occurs at the early stages of growth when a shell is relatively thin. A naive linear extrapolation of the data in Fig. 4.3 suggests that ID/OD would reach the ideal value for a starting particle diameter of ∼30 nm. Cobalt nanocrystals of this size, however, are ferromagnetic and aggregate into linear chains in solution. Thus, when they are sulfidized, particles tend to fuse together at the same time that the hollowing process occurs.

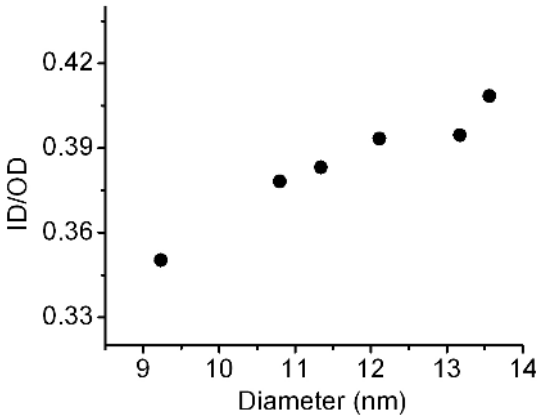

Figure 4.3: Relative void size increases with size of the starting particles for hollow nanostructure formation. The vertical axis shows the average value for the ratio of void diameter to outer shell wall width measured for a particular synthesis. The horizontal axis shows the average value of the particle diameter for the starting metallic particles.

Using non-spherical starting particles can, in principle, yield non-uniform shell thickness due to enhanced reactivity and diffusivity at corners and edges of the particle-shell interface, but we did not observe such an effect using disk-shaped cobalt particles as

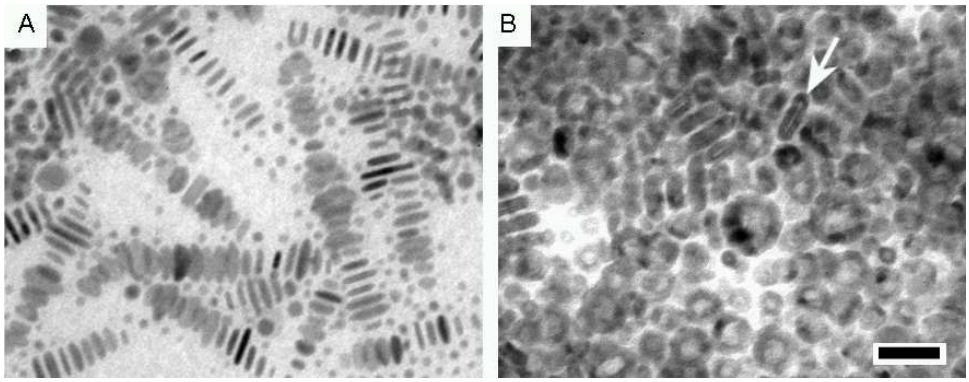

Figure 4.4: Sulfidation of hcp−Co nanodisks leads to formation of disk-shaped hollow boxes. The sulfidized disks have a reduced propensity to stack. Disks standing on side (one marked with an arrow) show that shell thickness is quite uniform over the whole disk surface. The scale bar is 50 nm.

starting materials. As shown in Fig. 4.4, at first glance, most sulfide particles derived from Co disks appear to be spherical hollow particles. However, more careful examination of the picture shows some hollow disk shaped boxes viewed edge on. The void diameter and shell thickness for the apparently spherical particles are similar to values measured for disk-shaped particles. This leads us to conclude that all hollow particles in the image are hollow disks, with some happening to lie flat on the substrate. The reduced propensity of disks to stack and stand on their side following sulfidation is explained by the absence of ferromagnetic attraction between them. Statistics on the sample produced at 120°C shows the change of size for the population of particles as the sulfidation reaction proceeds: the distribution of outer diameters progressively becomes skewed towards smaller diameters (Fig. 4.5). This change in shape distributions precedes the appearance of a significant fraction of Co_3S_4 in the diffraction pattern. We did not collect data on the ID distribution at these conditions and thus cannot compare volume distributions; still, the change of shape remains visible upon comparing distributions of the cube of OD at different times. Fracture of thicker shells as a consequence of stress build-up during growth would remove shells from the high end of the outer diameter distribution and explain the observation. Since further

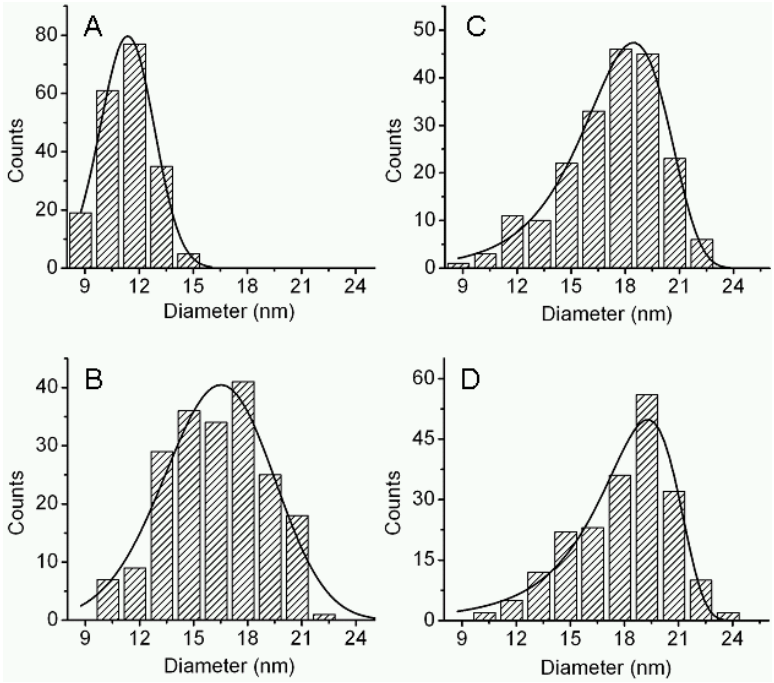

Figure 4.5: Evolution of particle size distribution at 120°C (A) Diameter distribution for the original $\epsilon-$Co nanospheres. Outer diameter distribution of sulfide shells obtained (B) 45 sec, (C) 5 min, (D) 25 min. The Co/S molar ratio used is 3:4. XRD verified particles measured for (B-D) to dominantly belong to the Co_9S_8 phase.

lowering of temperature to 100°C leads to partially fractured particles in TEM images (Fig. 4.2), it is reasonable to conclude that the tendency of shells to fracture becomes progressively stronger as temperature is lowered in the temperature range 70-180°C.

4.3 Sequential Phase Changes

XRD analysis of the reaction at 120°C indicates that the Co_9S_8 phase is kinetically favored although Co_3S_4 is the thermodynamically stable phase at the reaction conditions. Fig. 4.6c shows XRD patterns of aliquots taken out from a reaction with a sulfur-to-cobalt ratio of 4:3 at 120°C (same sample as shown in Fig. 4.1B). The aliquots were taken out from the hot synthesis solution with a syringe and rapidly injected into an equal volume of anhydrous methanol solution stored under argon at room temperature. After 45 seconds,

only Co_9S_8 can be clearly observed by XRD since the remaining Co core is now so small and/or amorphized that its diffraction peaks greatly broaden (Fig. 4.6a).

As the reaction proceeds, Co_9S_8 remains the major phase until the Co core is completely consumed at 25 minutes (Fig. 4.6b,c). Co_3S_4 has become the dominant phase by 125 minutes, and the change is evidenced by progressive shifting of the major peak position in the patterns as the highest intensity peaks for the two phases overlap, but are ideally offset by ∼4°C (Fig. 4.6d). The product collected after 19 hours has been completely converted into Co_3S_4 (Fig. 4.6e). These results indicate that the formation of Co_3S_4 hollow nanocrystals goes through two separate steps. The first step is the hollowing of cobalt nanocrystals by the outward diffusion of cobalt atoms to form Co_9S_8. The second step is the further transformation of Co_9S_8 to Co3S4 while retaining the hollow morphology. When the same reaction occurs at higher temperatures, the two-step nature of the transformation might be preserved but the intermediate Co_9S_8 particles would be difficult to observe due to the greatly increased reaction and diffusion rate. It is interesting that neither for the reactions performed at 120°C, nor for those performed at 182°C, simultaneous presence of three phases (i.e. Co, Co_9S_8, Co_3S_4) can be detected. This is in contrast to experimental and theoretical findings for bulk or micron

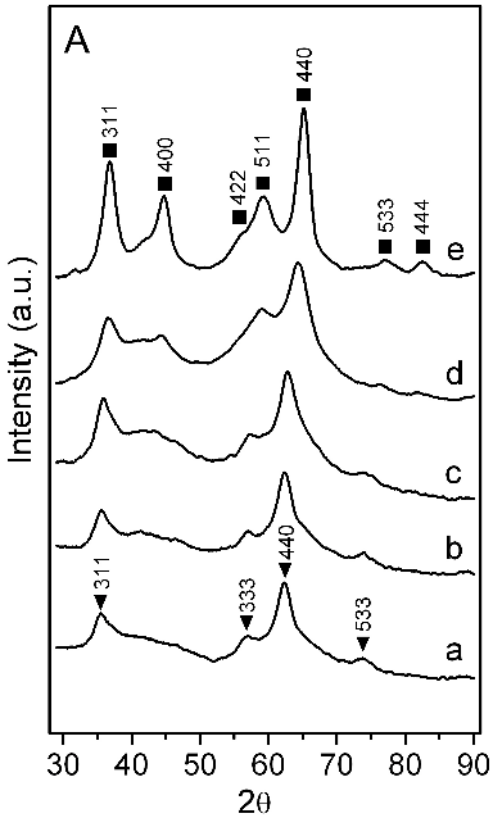

Figure 4.6: XRD patterns of the sample obtained from the solution after sulfidizing Co nanocrystals at 120°C for (a) 45 sec, (b) 5 min, (c) 25 min, (d) 125 min, (e) 19 hrs. Note that patterns (a-c) correspond to the same syntheses for which size statistics are provided for in Fig. 4.5. Co_9S_8 peaks are labeled in (a) and Co_3S_4 peaks are labeled in (e).

scale oxidation/sulfidation where a scale of multiple phases is expected to develop. In thin film growth, absence of some phases predicted by the phase diagram is known to occur; presumably the similar observation in the hollow nanoshells has an analogous explanation.

A similar phase change was induced when Co_9S_8 nanocrystals in solution were oxidized by refluxing at 182°C with an O_2/Ar mixture bubbling through. The crystallinity of the nanocrystals decreases dramatically at the onset of the phase transformation. After 5 minutes of exposure to O_2, Co_9S_8 peaks have largely disappeared with only the major (440) peak observable (Fig. 4.7). At the same time, the (440) peak of Co_3S_4 starts to appear. The peak intensity of Co_3S_4 continues to increase while the Co_9S_8 keeps decreasing. After 75 min, no Co_9S_8 can be detected. Further heating of the sample with O_2/Ar flow simply improves the crystallinity of the Co_3S_4 nanocrystals and leads to the appearance of two small peaks of CoO, suggesting that the following chemical reaction occurred:

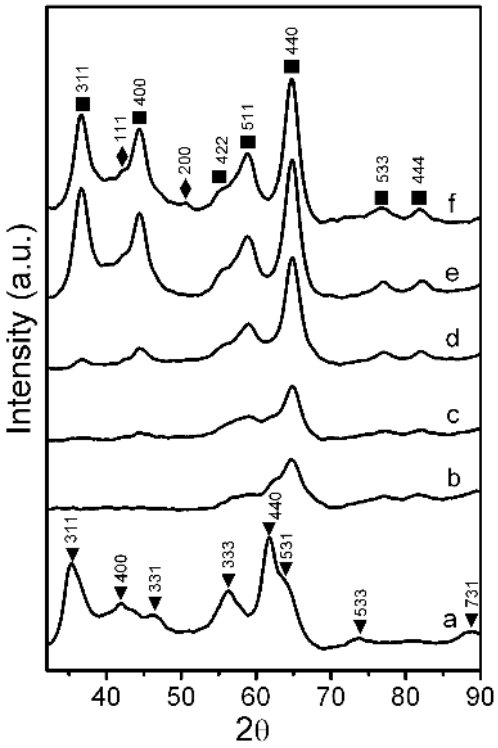

Figure 4.7: (XRD patterns of the sample obtained by heating a Co9S8 hollow nanocrystal solution at 182 C with a stream of O2/Ar (1:4 in volume ratio, 120 ml/min) mixture blowing through for (a) 0 min, (b) 5 min, (c) 15 min, (d) 75 min, (e) 135 min, and (f) 315 min.

$$2Co_9S_8(s) + 3O_2(g) \rightarrow 4Co_3S_4(s) + 6CoO(s)$$

Assuming that a Co_9S_8 shell transforms into a Co_3S_4 shell with a conformal coating of CoO layer, oxidation of a 4.5-nm thick Co_9S_8 shell is expected to yield a 4 nm thick Co_3S_4 shell with a 1 nm CoO coating. If the domain size is equal to the shell thickness for each compound, we should not be able to observe distinct oxide peaks due to extensive

size-broadening.

This conclusion is consistent with the fact that no oxide can be detected upon completion of the phase transformation at 75 min. The detection of CoO peaks after prolonged heating indicates significant increase CoO of domain size upon annealing. The intensities of CoO diffraction peaks are weak in comparison to those of Co_3S_4 which is consistent with the smaller volume of CoO formed and its relatively low X-ray scattering power. The hollow nanocrystals before and after oxidation were investigated by TEM. No significant size change was observed, although closer inspection suggests that shells tend to contain fewer grains in the final sample. Given the XRD results, the increased crystallinity is likely due to annealing at high temperature. We also attempted to perform a chemical reduction of the Co_9S_8 hollow nanocrystal dispersion by refluxing at 182°C with an H_2/Ar mixture flowing through. No phase and size change were observed after the sample was heated for 3 hours. The observed sharpening of XRD peaks with time is readily explained by annealing of the particle at high temperature, lowering average defect density and/or number of grains comprising the shells.

4.4 Summary

TEM images presented here show significant slowing of void coalescence at low temperatures such that formation of visible voids lags far behind complete consumption of Co cores. This is consistent with the observed porosity being due to a Kirkendall-type process operating in confined nanoscale geometries. Other mechanisms proposed to account for emergence of hollow or ring-like structures (e.g. upon oxidation of metal islands on supports) cannot explain the evolution of void morphology with time as a function of temperature in a natural way. Interestingly, formation of voids throughout a porous shell would seem to require that removal of Co cations from the core material not always proceed in a simple manner from the outer surface of the core inwards. It is quite possible that at

these lower temperatures, we are seeing some evidence of either statistical or electric-field driven effects, leading to a behavior different than what is seen in bulk.[71]

Despite the overall dominance of outward Co transport that leads to void formation, particle statistics demonstrate that significant inward growth and/or deformation of the sulfide shells also occurs through growth. Specifically, it is the magnitude of the void size, characterized either in relation to the average starting particle or as an average of ID/OD for the final product, that demonstrates that the inner boundary of the shell has retreated 1-2 nm from the original cobalt-solution interface. The observed decrease of ID/OD upon increasing starting Co particle size strongly suggests that the inward growth occurs mostly during the early stages of the growth process. The uniformity of the shell thickness as well as near-elimination of the void along the axial direction upon sulfidation of Co disks suggests that both anion and cation mobilities are high during the formation of the first 2-3 nm of sulfide shells, strongly recalling the presence of a reaction zone suggested for cation-exchange reactions performed on nanocrystals. Other justifications may also be involved in the observed inward relaxation; for example, as the synthesis proceeds, initially porous paths allowing for sulfur transport could become sealed or annealed out. In fact, an explanation involving moderate annealing at the synthesis temperature would also explain why an apparent 15% porosity can be seen in thicker shells obtained at 182°C despite the apparent absence of any porosity for thinner shells. Alternatively, compressive stresses created during the growth process may be sufficient to deform the sulfide shells when they are thinner. It is quite likely that a combination of processes determine the extent of inward growth.

Another deviation from behavior extrapolated from bulk studies involves the transformation of Co to Co_3S_4. In bulk sulfidation, the sulfide films support multiple phases, with a progression from cobalt-rich to sulfur-rich phases as one moves outwards from the cobalt-vapor interface. In contrast, X-ray diffraction characterization suggests a two-step transformation where the final product, Co_3S_4 does not appear until all cobalt has dis-

appeared. Since diffraction would not be sensitive to amorphous or very highly defected domains of Co or Co_3S_4, this finding may merit, in the future, verification with a chemically sensitive technique. However, at least in the case of Co_3S_4, one can argue that it is likely to nucleate in relatively defect-free domains: The transformation of a Co_9S_8 shell into a Co_3S_4 shell may be facilitated by the identical arrangement of sulfur anions in the two structures except for a slightly larger separation of the anions in Co_3S_4.

We have provided a number of observations which, when taken together, raise the possibility of propensity of shells to fracture within a range of the synthesis temperature. Small solid fragments of cobalt sulfide are present, to some extent, at all synthesis temperatures we have studied; however, apparently disintegrating shells in TEM images (for synthesis at 100°C) and statistically significant changes in the skewness of the shell volume distribution are only seen at a lower (120°C) temperature. A natural explanation is that fracture occurs, to some degree, over the complete temperature range that we have studied, but that higher temperatures result in relaxation of growth stresses and improve the adhesion between the core and the shell. The particles obtained at room temperature do not follow this proposed trend: no signs of fracture are seen in TEM images. However, given the very different mode of growth observed at this temperature, this may not necessarily contradict our interpretation. The calculated ratio of the volume of sulfide produced to the volume of cobalt consumed in the reaction is 2.4 for formation of Co_9S_8 and 3.1 for Co_3S_4. For oxidation of metals, this ratio is referred to as the Pilling-Bedworth ratio and is used as an empirical predictor of whether the metal oxide layer that forms on a metal surface will be a protective (passivating) or not. Most oxides with a value of Pilling-Bedworth ratio >2 develop large stresses during growth, leading to cracking, buckling or spalling. Presumably, the absence of such processes in bulk sulfidation experiments is due to relaxation of growth stresses at the higher temperatures ($\sim$900°C) used. The relatively large volume change upon sulfidation supports our interpretation of fracture during shell growth.

In summary, we investigated in detail the formation of cobalt sulfide hollow nanocrys-

tals through a Kirkendall-like mechanism in nanometer scale materials. Performing the reaction at 'high' (>120°C) temperature leads to fast formation of a single void inside each shell while reaction at room temperature leads to the formation of multiple voids, which can be attributed to strongly temperature-dependent diffusivities for vacancies. Although the void formation process is dominated by the outward diffusion of cobalt cations, there is still significant inward transport of sulfur anions as inferred from the fact that the inner diameter of the shell is smaller than the original cobalt nanocrystals. Also, as was discussed in the previous chapter, volume distributions for initial and final nanostructures imply that sulfide shells grown at high temperature contain extra volume comparing to the value calculated by assuming a single crystal material, indicating significant porosity and/or defective structure. At intermediate temperatures (100-120°C), we observe indirect and direct signs of fracture occurring upon during shell formation. In addition, in this temperature range, formation of the Co_3S_4 phase proceeds slowly enough to enable observation of a two step process: Co is sulfidized into Co_9S_8 which subsequently transforms into Co_3S_4. The physical mechanism behind inward growth of the shell might involve bulk deformations of the shell or transport of sulfur through cracks in the shell.

Chapter 5

Crystallographic Alignment in Assemblies of Magnetic Particles

Drying of colloidal solutions on a substrate yields diverse morphologies of particle aggregates that are dictated by the strength of interparticle interactions, solvent properties, drying rate and substrate-particle interactions. In the case of magnetic nanocrystals, magnetic interactions between nanocrystals may also become significant. The width of a domain wall in a magnetic metal is, within an order of magnitude, ~50 nm. Nanocrystals with dimensions much smaller than this value cannot support multiple magnetic domains. Thus, materials that are ferromagnetic in bulk form often display alignment of atomic dipoles along a single average direction within isolated nanocrystals; the collective dipole is then referred to as a superdipole. In general, there will be one or several axes within each nanocrystal along which the superdipole will preferentially lie. The strength of the coupling between these directions and the magnetic superdipole is determined by anisotropies, not only in the crystal structure, but also in surface magnetic properties and nanocrystal shape.[87] As a rule of thumb, particle superdipoles may be consider fixed within experimental times (t $>$ 1 sec.) when the energy barrier to rotation of the superdipole from one low-energy orientation to another exceeds $25k_BT$. In this case, the nanocrystals are referred to as being

ferrromagnetic. For a particle for which the barrier to superdipole rotation is $< 25k_BT$, the superdipole samples many low energy directions within experimental timescales, yielding a net vanishing magnetization for each nanocrystal in the absence of magnetic coupling between nanocrystals and an external field. The barrier to superdipole rotation in nominally spherical $\epsilon-$Co nanocrystals 9 nm in diameter has been measured to be $\sim 5k_BT_{room}$.[87]

Larger magnetic nanocrystals tend to assemble into one-dimensional structures, like chains and loops, upon drying on a substrate.[88] This may be at least partially attributed to magnetic interactions between these particles. Large magnetic nanocrystals tend to be ferromagnetic due to a magnetocrystalline energy that scales with nanocrystal volume. Neglecting exchange effects between nanocrystals in contact, the fixed superdipoles may be treated as classical magnetic dipoles; loop-closing by forming chains and loops out of superdipoles minimizes magnetostatic energy. In contrast, smaller superparamagnetic nanocrystals, with vanishing time-averaged moments, form close-packed mono- and multilayer structures that are also known to be formed upon aggregation of non-magnetic particles.[32] Note that close-packed does not necessarily refer to hexagonal or face-centered cubic phases: if the nanocrystals are non-spherical or highly faceted, packing interactions may drive formation of more complex crystallographic phases in the aggregates instead.

Here, we present very briefly our observations, using electron microscopy, of assembly formation and emergence of orientational ordering in these assemblies. The conclusions are speculative, but turn out to be worthy of further study when the results are considered in detail.

5.1 Previous Results from the Literature

Assemblies of nanocrystals formed upon drying of colloidal solutions have been well studied. When tight size distributions are achieved for colloidal particles, an impressive degree of translational order can emerge in aggregates.[3,89] Periodic lattices of nanocrystals

thus formed are called 'superlattices' or 'supercrystals'. Not only classical close packed phases, but analogues of binary phases have been observed in superlattices.[90,91] Conventional TEM imaging as well as small angle electron diffraction can be used to verify that translational order spanning domains hundreds to thousands of nanometers in size.[20,92]

Nanocrystals in two- or three-dimensional superlattices typically are randomly oriented with respect to each other crystallographically. Wide angle electron diffraction patterns obtained from these aggregates show continuous rings corresponding to a powder of randomly oriented crystallographic domains. Rare reports of collective alignment of atomic lattices of individual nanocrystals in aggregates and superlattices exist in the literature. Many of these observations are of faceted particles forming two-dimensional arrays where alignment of particle facets is evident in TEM images; observation of breaking of radial symmetry in diffracted intensity may also be observed if orientational order is long-ranged. In most cases, the crystallographic axis pointing out of plane is a high symmetry axis, so that in the case of perfect matching of facets, nanocrystals form a single orientational domain.[48,92,93]

A study by Wang illustrating the existence of several distinct packing arrangements in superlattices of 11 nm $\epsilon-$Co nanocrystals deserves special mention.[94] A uniform faceted shape for the constituent $\epsilon-$Co nanocrystals was proposed to allow realization of the multiple observed phases. In TEM images of these superlattices, orientational defects between neighboring supercrystals domains are seen to be quite common. The defects should suppress long-range orientational order and lead to powder-like electron diffraction patterns. On the other hand, orientational domains should be visible in dark-field images formed by selecting an arc on a continuous diffraction ring. No dark field images were provided by Wang; it is not clear whether this is due to an instrumental limitation, the assemblies being too thick for dark field imaging or to weak crystallographic co-alignment of neighbors within a single domain. Interestingly, our observations of aggregates of smaller, 9 nm $\epsilon-$Co nanocrystals show predominantly close packed arrangements, suggesting a weaker

overall role for faceting in determining superlattice morphology. Dark field images of our assemblies also suggest that orientational defects are common. Yet, the variation of dark-field intensity imply that common crystallographic axes within individual nanocrystals align, *on average* , into patterns that sometimes span whole assemblies. Emergence of average long-range orientational order, despite relatively weak short range alignment, raises the possibility of long-range collective interactions playing a role during the formation of the assemblies.

5.2 Collective Alignment in Assemblies of Cobalt Nanocrystals

Spherical $\epsilon-$Co nanocrystals of 9 nm diameter were prepared according to procedures outlined in Ch. 2. A single size selection step was employed to remove any smaller nanocrystals present in the as-synthesized solution. The precipitated, larger nanocrystals were redissolved in DCB. A drop of the solution was placed on a TEM grid and covered with a Petri dish. Slow evaporation of the solvent allowed formation of ordered aggregates of the nanocrystals. These aggregates differed in morphology depending on the synthetic batch and also varied, to a lesser extent, from TEM grid to TEM grid. One morphology commonly observed was that of the multilayered 'islands' shown in Fig. 5.1A&B.

By using an aperture to select an area containing exactly one island, it is possible to acquire diffraction patterns arising largely from nanocrystals comprising that island. In some samples, the majority of islands produced patterns corresponding to a *non-random* orientation distribution for crystallographic axes of the nanocrystals. Specifically, several diffraction rings show concentration of intensity into spots which display apparent sixfold symmetry (Fig. 5.1C). It is tempting to consider the apparent threefold symmetry to indicate presence of nanocrystals with a single common crystallographic alignment; in this case, a threefold symmetry axis of the $\epsilon-$Co structure would have to point along the electron

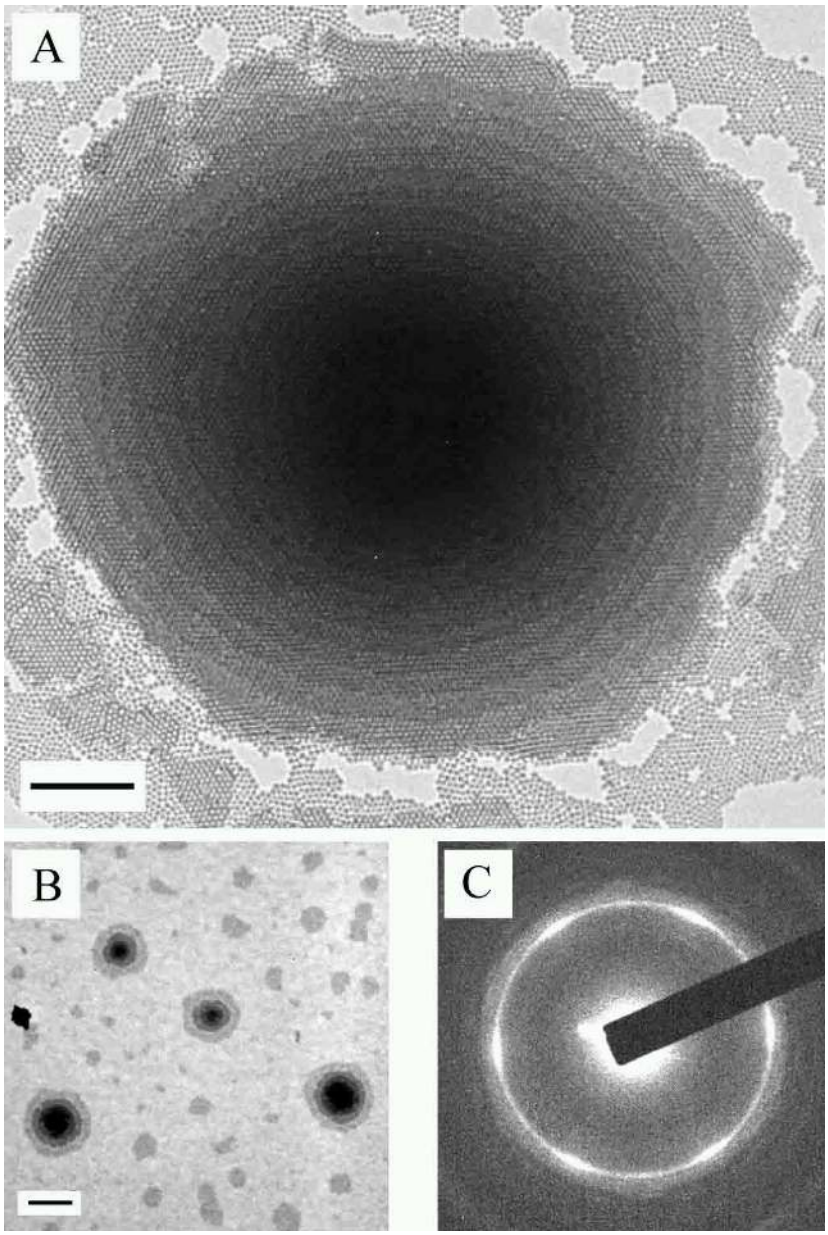

Figure 5.1: (A) Transmission electron micrograph of a multilayered cobalt nanoparticle island. (B) Low magnification TEM image displaying multiple islands, as well as small patches of nanoparticle monolayers. (C) SAED from island in (A), displaying the ϵ-Co $\{221\}$ reflection. Note the non-uniform intensity around the ring. Scalebars are both 2 μm. Figures courtesy of D. Aruguete.

beam. We have simulated all such possible cases using the Cerius II software package. No satisfactory fit to the pattern of the spots were found. In fact, the observed presence of six spots on the {221} ring, all rotated by 60° from its neighbor is incompatible with a single crystal diffraction pattern of the $\epsilon-$Co crystal structure. Thus, multiple discrete orientations must exist for the nanocrystals comprising the islands. Whether these orientations are random from one nanocrystal to the next or whether particles of common orientations form large domains is a question that cannot be answered by selected area electron diffraction.

Dark field microscopy is an ideal tool to check for the existence of crystallographically oriented domains. In this mode of electron microscopy, images are formed from one selected spot on a diffraction ring; ideally only the particles giving rise to diffracted intensity in the selected area show up in the images. In practice, obtaining a good signal-to-noise ratio in images can be challenging; thus, we chose the brightest spots, located on the 221 ring. Most dark field images show weak and non-symmetrical variations, suggesting domains of weak alignment around an average orientation. In very rare cases, however, the data suggests *strong* alignment of crystallographic domains into a vortex-like structure that spans the whole island. (Fig. 5.2). For each selected {221} spot in the diffraction pattern, a lobe of maximal intensity is observed in the corresponding image (Fig. 5.2A1-3). Each lobe in the images and the corresponding spot in the diffraction pattern lie along perpendicular directions. Reciprocal and real space directions coincide for a cubic crystal structure, such as $\epsilon-$Co. Thus, the relative alignments of diffraction spots and the corresponding regions of high intensity in the images suggest that $\langle 221 \rangle$ axes of individual nanocrystals align into six distinct domains, which in turn arrange into a loop spanning the entire island (Fig. 5.2B&C). Intensity in dark field images drops off near the center of the island. Profiles of corresponding bright field images show no comparably distinct drop-off; thus it is likely that this is indicative of reduced orientational order at the center of the islands. That is consistent with a magnetic driving force underlying orientational alignment as the net magnetic force in a thick layer is expected to be weaker than one in a thin layer.

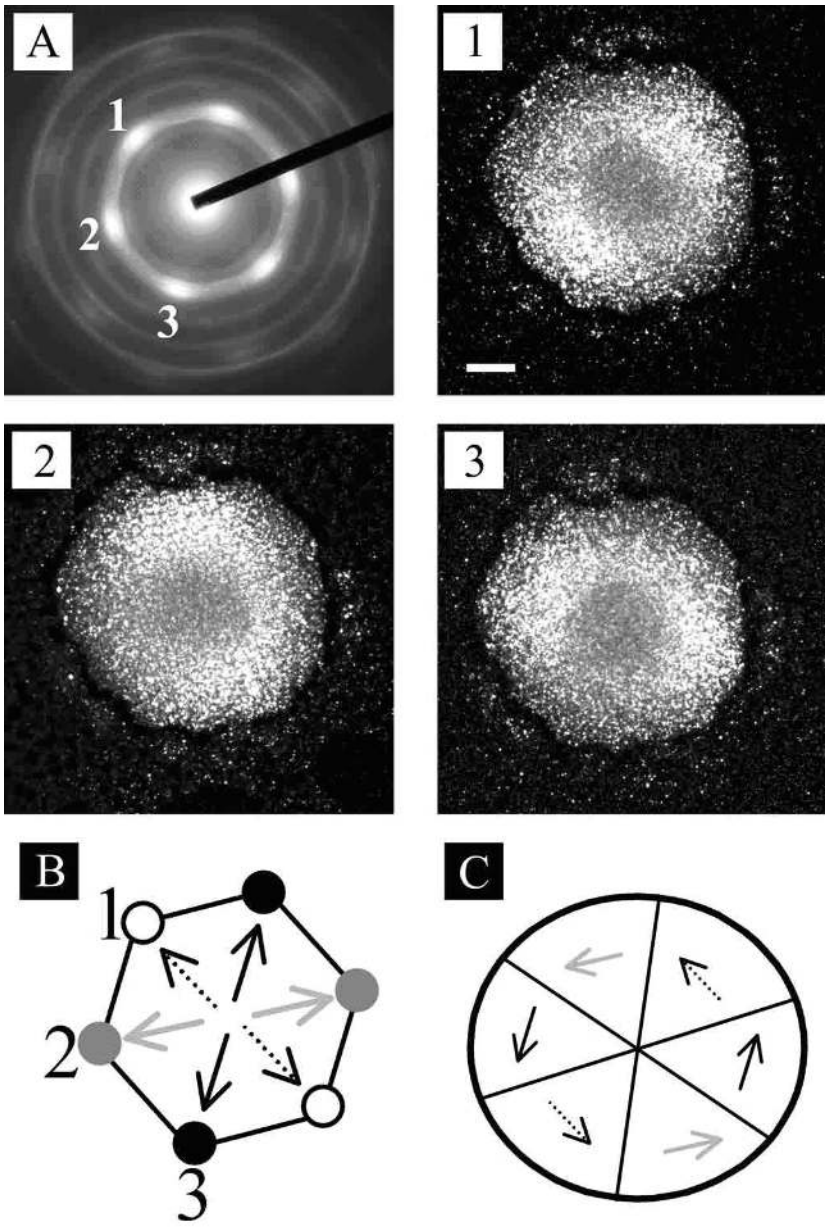

Figure 5.2: (A) Observation of strong preferred orientation in a Co nanoparticle island by SAED, and dark field TEM images formed from spots labeled 1, 2, and 3 on the diffraction pattern. (B) Schematic of the arrangement of {221} reflections in (A), with corresponding ⟨221⟩ vectors in real space. (C) Schematic of the island, in which the ⟨221⟩ vectors are mapped onto the corresponding areas of maximal intensity from the dark field images. Scalebar is 2μm. Figures courtesy of D. Aruguete.

5.3 Discussion of Possible Mechanisms

The emergence of vortex-like arrangements of a crystallographic axis in a nanocrystal aggregate could be due to magnetic loop-closing interactions among individual superdipoles. The interaction strength between a pair of dipoles (each with a moment of $4 \times 10^4 \mu_B$ chosen to match the measured saturation magnetization for $\epsilon-$Co) separated by 11 nm (corresponding to 9 nm particles with a 1 nm thick surfactant layer on each particle) turns out to be $E_M \sim k_B \times (1500K)$. Thus, in principle, the dipolar interaction between two particles in contact is strong enough to at least partially overcome thermal fluctuations at room temperature. Kinetic Monte Carlo simulations verify that mono- and multilayers of classical dipoles, approximating our nanocrystals' superdipoles, will display collective alignment of superdipoles at room temperature.[95] In a roughly circular island, this alignment takes the form of superdipoles arranging into a loop spanning the island. Thus, *magnetic* ordering in islands of $\epsilon-$Co nanocrystals is thermodynamically feasible at room temperature.

For magnetic ordering to translate into an alignment of the crystalline axes, the magnetocrystalline energy, E_C, per particle must be large enough to provide an observable correlation between the magnetic dipole and crystallographic orientation. Since $\epsilon-$Co has not been produced as a bulk phase, experimental values of the magnetocrystalline energy must be extracted from the magnetic relaxation kinetics of dilute nanoparticle solutions. The best value in the literature is $\sim$5 kT for a 9.5 nm $\epsilon-$Co particle.[87] Assuming a Boltzmann distribution, this coupling gives a FWHM of $\sim 40^\circ$ for the angle between the easy axis and the dipole direction, somewhat larger than the FWHM of $\sim 20^\circ$ observed for the diffracted intensity around a peak in our SAED diffraction patterns. It is likely that an undetected, slight faceting of our apparently spherical particles assists the alignment process, reducing the FWHM of the orientation distribution function to the experimentally observed values.

For a nanoparticle in contact with a monolayer of particles in a vortex state, the interaction energy between its dipole and the monolayer's field is $\sim E_M$. Far away from the monolayer (particle-monolayer separation r >> R, the monolayer radius), the interaction energy scales as r^{-7}. Therefore, orientation of the particle by the monolayer field must take place very close to the monolayer, e.g. r/d < 2, where d is the particle separation in the monolayer. It is possible to place some kinetic constraints on the monolayer growth process for orientational order to emerge. Assuming $E_C >> E_M > k_BT$, the correlation between the particle dipole and crystallographic coordinates becomes perfect. In that case, the magnitude of the torque orienting a particle with the monolayer, N, is due to the magnetic interaction energy and given by $N = MHsin\phi$, where ϕ is the angle between the position dependent magnitude of the field due to the monolayer, H, and the magnetic dipole, M, of the approaching particle. The maximum value for this torque is attained for a particle in contact with the monolayer and has magnitude $\sim E_M$. This torque gives rise to a rotational velocity, $\omega = N/\xi_r$, where ξ_r is the rotational friction constant for the particle. The order of magnitude for the time required for a particle to rotate to the minimum energy configuration is given by $t_R = \langle\phi/\omega(\phi)\rangle$, with the average taken over ϕ. For a rigid spherical nanoparticle of diameter d in a solvent of viscosity $\eta, \sigma_r = \pi\eta d^3$. Using d = 11 nm and η = 1.32 cP for 1,2-dichlorobenzene, we find t_R 0.3 μs. For comparison, using $\tau = f_0^{-1} exp(-E_C/k_BT)$ with $f_0 = 4 \times 10^9 s^{-1}$ as measured for 25 nm fcc-Co nanoparticles,,[96] the lifetime of a dipole orientation in zero field, τ, for a 9 nm $\epsilon-$Co particle will exceed t_R when $E_C \geq 7k_BT$. Thus by assuming a somewhat larger anisotropy energy (and/or magnetic moment density) for $\epsilon-$Co than measured previously, one predicts that the particle dipole is frozen to a single easy crystal axis within the timescale of particle rotation, enhancing the likelihood of successful alignment. For crystallographic alignment to emerge, each particle that attaches to a growing island must then remain free to rotate for a time exceeding t_R. A more realistic discussion of the kinetics is complicated by several factors. First, relevant energies and timescales turn out to be similar in magnitude ($E_M \sim E_C; \tau \sim t_R$). This makes it

difficult to make simplifications by considering a degree of freedom to be frozen or ergodically sampled during the process. Future computational work could address in detail the mutual evolution of the crystallographic and magnetic orientation of a particle subject to thermal fluctuations.[97] Secondly, since any orientation process would have to take place when the nanoparticle is in contact with the island, short-range interactions between particles are important.[98,99] Finally, in the experimentally observed multilayers, the deposition process might occur in a more complicated mode or geometry than discussed above.

Chapter 6

Conclusions and Speculations

6.1 Synthetic Control

The degree of control, in the multiple senses of reproducibility, tunability and homogeneity, over morphology of metallic nanocrystals has proven here to dictate tractability of processes that utilize them as starting materials. An anisotropic disk-like particle shape was achieved through the use of a surfactant which likely binds to specific crystal facets. Unfortunately, samples of hcp−Co nanodisks produced were neither morphologically nor crystallographically homogeneous. Interestingly, the very broad distributions observed for diameters of hcp−Co nanodisks, could be arising from a geometrical factor: a cylindrical particle confined largely to 2D growth in the disk-plane theoretically should not exhibit 'size-focusing'. A comparison of growth of nanodisks vs. nanospheres of the same material, prepared by use of a differing surfactant mixture, may thus merit attention; signicant refinement of sample homogeneity over that shown for hcp−Co nanodisks will be required for such studies.

Several problems described in Chapter 2 may be attributed to a weak degree of control over thermal history of samples, both during and following formation of Co nanocrystals in solutions. Thus, performing syntheses in smaller volumes (with decreased

thermal mass) and using well-defined temperature control algorithms is likely a fruitful avenue. Given that multiple crystalline phases may be achieved in the colloidal Co system with facile changes to the surfactant mixture, temperature or choice of precursors, branched or other complex nanostructures composed of this substance are likely to be produced in the near future.

6.2 Kirkendall-Like Processes

Within the cobalt sulfide system, we believe that significant inward growth or deformation of a shell occurs during the early stages of growth. As growth temperature is lowered, the final product becomes more complex: shell fracture may occur and/or multiple voids may be produced within each particle at lower temperatures. Alternative mechanisms may be proposed for many of our observations and further studies, both experimental and theoretical, are needed to arrive at a more conclusive understanding. We believe that the general concept of formation of hollow nanocrystals using the Kirkendall effect can be extended compositionally to the synthesis of diverse material classes including metals, semiconductors and insulators. Furthermore, the production of hollow disk shaped boxes that we presented indicates that the procedure reproduces the shape of the original nanocrystals in the final porous product. Utilizing starting materials where shape control has been established, forming hollow particles and chemically modifying the product using procedures that preserve particle porosity and morphology, it should be possible to combine a strong degree of shape and compositional control in the production of hollow nanostructures.

A better understanding of the mode of growth should assist future efforts to extend synthetic control over geometrical, thermodynamic or crystallographic properties of similarly prepared hollow nanostructures, which may find uses in fields as diverse as catalysis, ultrasound imaging, low-dielectric materials and drug delivery.

6.3 Assemblies of Magnetic Particles

Aggregation of $\epsilon-$Co nanocrystals within a narrow size range was observed to result in aggregates where crystallographic axes of individual nanocrystals commonly adopted one of a few specific orientations. This is seen specifically in electron diffraction patterns obtained from the aggregates. In very rare cases, it was possible to obtain dark-field images of aggregates showing large domains of a single average orientation. The simplest interpretation of the data in such cases suggests that a common crystallographic axis forms radial loops in an aggregate. This raises the intriguing possibility that magnetic loop-closing interactions between nanocrystals can be sufficiently strong to play a role during assembly formation.

Our experimental findings raise the possibility that it may be generally possible to realize crystallographic alignment through interparticle magnetic interaction, even in the absence of an applied field. When nanocrystals are composed of $\epsilon-$Co, a relatively soft, but high moment magnetic material, interparticle interactions are sufficiently high for loop-closing interactions to overcome thermal fluctuations at room temperature. Furthermore, the torques between nominally superparamagnetic nanocrystals turn out to be sufficiently large that these particles may be considered to be ferromagnetic over the timescales required for co-alignment of the particles in solvent. On the other hand, increasing strength of dipolar interactions above a critical threshold (e.g. by utilizing larger or higher moment nanocrystals) may inhibit emergence of orientational order by driving non-equilibrium aggregation of nanocrystals. Theoretical analysis and stochastic simulations of formation of aggregates may shed some light on the precise nature of the trade-offs involved.

Bibliography

[1] V. LaMer and R. Dinegar, Journal Of The American Chemical Society **72**, 4847 (1950).

[2] H. Nakamura and M. Shiga, Physica B **237**, 453 (1997).

[3] C. Murray, C. Kagan, and M. Bawendi, Annual Review Of Materials Science **30**, 545 (2000).

[4] C. Murray, D. Norris, and M. Bawendi, Journal Of The American Chemical Society **115**, 8706 (1993).

[5] X. Peng, M. Schlamp, A. Kadavanich, and A. Alivisatos, Journal Of The American Chemical Society **119**, 7019 (1997).

[6] X. Peng *et al.*, Nature **404**, 59 (2000).

[7] L. Manna, E. Scher, and A. Alivisatos, Journal Of The American Chemical Society **122**, 12700 (2000).

[8] L. Manna *et al.*, Nature Materials **2**, 382 (2003).

[9] D. Milliron *et al.*, Nature **430**, 190 (2004).

[10] A. Alivisatos, Journal Of Physical Chemistry **100**, 13226 (1996).

[11] J. Turkevich, P. Stevenson, and J. Hillier, Discussions Of The Faraday Society 55 (1951).

[12] G. Schmid, Chemical Reviews **92**, 1709 (1992).

[13] M. Brust *et al.*, Journal Of The Chemical Society-Chemical Communications 801 (1994).

[14] C. Murray, S. Sun, H. Doyle, and T. Betley, MRS Bulletin **26**, 985 (2001).

[15] S. Folsch, P. Hyldgaard, R. Koch, and K. Ploog, Physical Review Letters **92**, (2004).

[16] Y. Xia and N. Halas, MRS Bulletin **30**, 338 (2005).

[17] R. Narayanan and M. El-Sayed, Journal Of Physical Chemistry B **109**, 12663 (2005).

[18] F. Stellacci, Nature Materials **4**, 113 (2005).

[19] Y. Yin and P. A. Alivisatos, Nature **439**, 664 (2005).

[20] C. Desvaux *et al.*, Nature Materials **4**, 750 (2005).

[21] Y. Yin *et al.*, Science **304**, 711 (2004).

[22] A. Smigelskas and E. Kirkendall, Transactions Of The American Institute Of Mining And Metallurgical Engineers **171**, 130 (1947).

[23] D. Porter and K. Easterling, *Phase Transformations In Metals And Alloys*, 2nd ed. (Chapman And Hall, London, 1992), pp. 89–90.

[24] T. Hyeon, Chemical Communications 927 (2003).

[25] M. Green, Chemical Communications 3002 (2005).

[26] E. Shevchenko *et al.*, Journal Of The American Chemical Society **125**, 9090 (2003).

[27] X. Wang, J. Zhuang, Q. Peng, and Y. Li, Nature **437**, 121 (2005).

[28] H. Reiss, Journal Of Chemical Physics **19**, 482 (1951).

[29] T. Sugimoto, Advances In Colloid And Interface Science **28**, 65 (1987).

[30] X. Peng, J. Wickham, and A. Alivisatos, Journal Of The American Chemical Society **120**, 5343 (1998).

[31] O. Vidoni *et al.*, Angewandte Chemie-International Edition **38**, 3736 (1999).

[32] I. Lisiecki and M. Pileni, **19**, 9486 (2003).

[33] A. Taleb, C. Petit, and M. Pileni, Chemistry Of Materials **9**, 950 (1997).

[34] C. Petit, A. Taleb, and M. Pileni, Advanced Materials **10**, 259 (1998).

[35] V. F. Puntes, D. Zanchet, C. K. Erdonmez, and A. P. Alivisatos, Journal Of The American Chemical Society **124**, 12874 (2002).

[36] F. Dumestre *et al.*, Angewandte Chemie-International Edition **41**, 4286 (2002).

[37] J. Thomas, Journal Of Applied Physics **37**, 2914 (1966).

[38] P. Hess and P. Parker, Journal Of Applied Polymer Science **10**, 1915 (1966).

[39] E. Papirer *et al.*, Journal Of Colloid And Interface Science **94**, 207 (1983).

[40] J. Chen, C. Sorensen, K. Klabunde, and G. Hadjipanayis, Journal Of Applied Physics **76**, 6316 (1994).

[41] C. Gibson and K. Putzer, **267**, 1338 (1995).

[42] K. Shafi, A. Gedanken, and R. Prozorov, Advanced Materials **10**, 590 (1998).

[43] A. Holzwarth, J. Lou, T. Hatton, and P. Laibinis, Industrial & Engineering Chemistry Research **37**, 2701 (1998).

[44] S. Sun and C. Murray, Journal of Applied Physics **85**, 4325 (1999).

[45] D. Dinega and M. Bawendi, Angewandte Chemie-International Edition **38**, 1788 (1999).

[46] C. Petit, A. Taleb, and M. Pileni, Journal Of Physical Chemistry B **103**, 1805 (1999).

[47] V. F. Puntes, K. M. Krishnan, and A. P. Alivisatos, **291**, 2115 (2001).

[48] C. Murray *et al.*, IBM Journal Of Research And Development **45**, 47 (2001).

[49] B. Canals and C. Lacroix, Physical Review B **61**, 11251 (2000).

[50] D. Hobbs and J. Hafner, Journal Of Physics-Condensed Matter **13**, L681 (2001).

[51] M. Bawendi, A. Kortan, M. Steigerwald, and L. Brus, Journal Of Chemical Physics **91**, 7282 (1989).

[52] B. Hall and R. Monot, Computers In Physics 414 (1991).

[53] J. Wickham, A. Herhold, and A. Alivisatos, Physical Review Letters **84**, 923 (2000).

[54] A. Guinier, *X-ray diffraction in crystals, imperfect crystals, and amorphous bodies* (Dover, New York, 1994).

[55] W. Tseng, C. Hsu, C. Chi, and K. Teng, Materials Letters **52**, 313 (2002).

[56] D. Yang, J. Gillet, M. Meunier, and E. Sacher, Journal Of Applied Physics **97**, 024303 (2005).

[57] H. Zhang, B. Gilbert, F. Huang, and J. Banfield, **424**, 1025 (2003).

[58] J. Tang, M. Myers, K. Bosnick, and L. Brus, Journal Of Physical Chemistry B **107**, 7501 (2003).

[59] D. Son, S. Hughes, Y. Yin, and A. Alivisatos, **306**, 1009 (2004).

[60] F. Freund, A. Staple, and J. Scoville, Proceedings Of The National Academy Of Sciences Of The United States Of America **98**, 2142 (2001).

[61] V. Buscaglia and C. Milanese, Journal of Physical Chemistry B **109**, 18475 (2005).

[62] S. Mrowec, M. Danielewski, and A. Wojtowicz, Journal Of Materials Science **33**, 2617 (1998).

[63] D. Williams and C. Carter, *Transmission Electron Microscopy* (Plenum, New York, 1996), p. 150.

[64] S. Mrowec, S. Rusiecki, and A. Wojtowicz, Bulletin Of The Polish Academy Of Sciences-Chemistry **34**, 411 (1986).

[65] M. Danielewski, S. Mrowec, and A. Wojtowicz, Oxidation Of Metals **35**, 223 (1991).

[66] S. Mrowec, M. Danielewski, and A. Wojtowicz, Bulletin Of The Polish Academy Of Sciences-Chemistry **41**, 305 (1993).

[67] S. Mrowec and K. Hashimoto, Journal Of Materials Science **30**, 4801 (1995).

[68] H. Nakajima, JOM-Journal Of The Minerals Metals & Materials Society **49**, 15 (1997).

[69] G. B. Gibbs, Oxidation of Metals **16**, (1980).

[70] G. B. Gibbs, Oxidation of Metals **7**, 173 (1973).

[71] F. Aldinger, Acta Metallurgica **22**, 923 (1974).

[72] E. Derouane, J. Chludzinski, and R. Baker, Journal Of Catalysis **85**, 187 (1984).

[73] 2003, online database, URL: http://www.knovel.com/knovel2/Toc.jsp?BookID=761.

[74] S. R. Shatynski, Oxidation of Metals **11**, 307 (1977).

[75] L. Guo and C. J. Murphy, Nano Letters **3**, 231 (2003).

[76] D. Farrell, S. A. Majetich, and W. J. P, Journal of Physical Chemistry B **107**, 11022 (2003).

[77] H. J. Fan *et al.*, Solid State Communications **130**, 517 (2004).

[78] Y. Sun and Y. Xia, Science **298**, 2176 (2002).

[79] Y. Sun, M. B. T, and Y. Xia, Nano Letters **2**, 481 (2002).

[80] R. A. Masamura, B. B. Rath, and P. C. S, Acta Materialia **50**, 4535 (2002).

[81] J. Zenisek, J. Svoboda, and F. F. D, Philosophical Magazine **85**, 2363 (2005).

[82] K. Wu, J. Morral, and Y. Wang, Acta Materialia **52**, 1917 (2004).

[83] T. Campbell *et al.*, Physical Review B **71**, 205413 (2005).

[84] Q. Li and R. Penner, Nano Letters **5**, 1720 (2005).

[85] J. Tracy, D. Weiss, D. Dinega, and M. Bawendi, Physical Review B **72**, 064404 (2005).

[86] B. Liu and H. Zeng, Journal Of The American Chemical Society **126**, 16744 (2004).

[87] G. Held *et al.*, Physical Review B **6401**, art. no. (2001).

[88] D.-B. R. Tripp SL and W. A, Angewandte Chemie-International Edition **42**, 5591 (2003).

[89] C. Collier, T. Vossmeyer, and J. Heath, Annual Review Of Physical Chemistry **49**, 371 (1998).

[90] F. Redl, K. Cho, C. Murray, and S. O'Brien, **423**, 968 (2003).

[91] E. Shevchenko *et al.*, Journal Of The American Chemical Society **124**, 11480 (2002).

[92] F. Dumestre *et al.*, Science **303**, 821 (2004).

[93] D. Kang, J. Lee, F. Papadimitrakopoulos, and M. Aindow, Philosophical Magazine Letters **83**, 569 (2003).

[94] Z. Wang, Z. Dai, and S. Sun, Advanced Materials **12**, 1944 (2000).

[95] J. E. Moore.

[96] W. Wernsdorfer, E. Orozco, and e. a. Hasselbach K, Physical Review Letters **78**, 1791 (1997).

[97] J. Garcia-Palacios and F. Lazaro, Physical Review B **58**, 14937 (1998).

[98] E. Rabani and S. Egorov, Journal of Chemical Physics **115**, 3437 (2001).

[99] U. Landman and W. D. Luedtke, Faraday Discussions **125**, 1 (2004).